A deeper understanding of flooding dynamics in gas diffusion electrodes for CO2 electrolyzer: how interfacial pressure shapes gas–liquid stability

Chemical Engineering Journal 527 (2026) 171393

Contents lists available at ScienceDirect

Chemical Engineering Journal

journal homepage: www.elsevier.com/locate/cej

A deeper understanding of flooding dynamics in gas diffusion electrodes for CO_2 electrolyzer: how interfacial pressure shapes gas–liquid stability

Santiago Quesada [a,b], Laura Gatti [a,b], Matteo Alberghini [c,*], Alessio Tommasi [c], Marco Etzi [a], Alessio Mezza [a], Adriano Sacco [a], Fabrizio C. Pirri [a,b], Daniele Sassone [a,*]

[a] Center for Sustainable Future Technologies @POLITO, Istituto Italiano di Tecnologia, Via Livorno 60, 10144, Turin, Italy
[b] Department of Applied Science and Technology, Politecnico di Torino, C.so Duca degli Abruzzi 24, 10129, Turin, Italy
[c] Gemmate Technologies, via Reano 31, 10090, Buttigliera Alta, Italy

ARTICLE INFO

Keywords:
CO_2RR
Flooding
Perspiration
Backpressure
Interface
Flow cell
MEA
Multiphysics analysis

ABSTRACT

Gas-fed CO_2 electrolyzers are a promising technology for sustainable fuel and chemical production, but their industrial deployment is limited by the instability of gas diffusion electrodes (GDEs), particularly in microfluidic flow cells (MFCs). A key failure mechanism is electrode flooding, which discontinues CO_2 transport and favours hydrogen evolution. Although pressure control across the gas–liquid interface has emerged as a strategy to mitigate flooding, the precise role of differential pressure (ΔP) between gas and liquid side of the GDE remains poorly understood and inconsistently defined in literature. In this work, we systematically explore how gas and liquid pressure management alters the GDE interface, focusing on the understudied "*flow-by*" regime. Using Cu nanoparticles as a model catalyst and operating at industrially relevant current densities (0.5 A cm^{-2}), we monitor flooding dynamics through real-time pressure readings, product selectivity analysis, electrochemical impedance spectroscopy (EIS) and field emission scanning electron microscopy (FE-SEM) in different electrochemical setups with several commercial Gas Diffusion Layers (GDL). Our results demonstrate that a ΔP of 30 mbar can fully suppress flooding, preserving catalyst performance and enabling selective CO_2 reduction for over 6 h at 0.5 A cm^{-2}, almost an order-of-magnitude improvement over uncontrolled system. The experimental ΔP value is confirmed by multiphysics simulations, by modelling capillary-driven liquid invasion and gas transport, in which a predicted onset value of 20 mbar is defined as the required value to prevent the flooding. This work provides the first integrated framework combining pressure tuning, diagnostics, and multi-physics simulation to define and optimize *flow-by* operation, offering actionable insights for designing robust, high-performance CO_2 electrolyzers.

1. Introduction

The rising atmospheric concentration of CO_2 is one of today's most urgent environmental challenges. Industrial activities, especially those involving fossil fuels, disrupt the natural carbon cycle and drive global warming through the greenhouse effect [1–3]. Emerging technologies now offer ways to capture CO_2 from concentrated sources or directly from the air [4]. When paired with conversion systems, these approaches can help regulate CO_2 levels and partially close the carbon loop.

Gas-fed electrolyzers directly convert CO_2 into value-added products [5] by means of two main electrochemical cell types: Microfluidic Flow Cells (MFCs), which use liquid electrolytes, and Membrane Electrode Assembly (MEA) cells, which operate without a liquid catholyte. Both rely on Gas Diffusion Electrodes (GDEs) to achieve high current densities (>300 mA cm^{-2}) [5] needed for industrial purpose. However, GDEs face serious degradation issues, especially at high currents, limiting the electrolyzers' operational lifetimes [6–8].

In MFCs, GDE "flooding" occurs when liquid infiltrates the microporous layer, blocking CO_2 diffusion to the catalyst and promoting the competing Hydrogen Evolution Reaction (HER) [9–12]. While GDEs are hydrophobic by design, electrowetting (charge redistribution caused by the applied potential) lowers the Liquid Entry Pressure (LEP), making them prone to flooding [6,13,14]. In MEAs, flooding is less severe, but pore clogging from bicarbonate salt precipitation (from CO_2 and OH^- reaction and cation migration from the anode) is more problematic. In

* Corresponding authors.
E-mail addresses: matteo.alberghini@gemmate-technologies.com (M. Alberghini), daniele.sassone@iit.it (D. Sassone).

https://doi.org/10.1016/j.cej.2025.171393
Received 9 September 2025; Received in revised form 19 November 2025; Accepted 28 November 2025
Available online 5 December 2025

both cases, the failure mechanism involves pore occlusion: either by liquid (flooding) or solid salts (crystallization). Several strategies have been developed to prevent flooding, including adding hydrophobic polytetrafluoroethylene (PTFE) particles in the catalyst layer (CL) [15,16], using PTFE membranes as GDE [17], applying differential pressure ΔP across the GDE [18], or removing the liquid phase entirely (MEAs).

Flooding arises from liquid–gas interfacial forces, strongly governed by pressure. Three regimes are typically defined: (1) *Gas breakthrough*, when gas bubbles penetrate the GDE, disrupting electrolysis, (2) *Liquid breakthrough*, when electrolyte floods the GDE, blocking CO_2 access, and (3) *Flow-by*, gas diffuses through while liquid remains mostly outside the GDE [19–22]. Flow-by is considered optimal for CO_2 reduction but its nature is unclear. Some define it as a non-flooded state [18], while others describe it as involving "perspiration" [7,22]: a controlled and mild electrolyte penetration that, despite slightly reducing CO_2RR selectivity, may help preventing bicarbonate salt accumulation [7,18,19,22]. Conversely, some argue that a completely dry GDE is unattainable without transitioning to gas breakthrough [21]. Further complexity arises from variations in Gas Diffusion Layer (GDL) types, which may or may not support flow-by. A clear distinction must be made between gas breakthrough and flow-by conditions. GDEs, often misrepresented as gas–solid–liquid (triphasic) systems [8], enhance CO_2 dissolution [23] near the catalyst, promoting diffusion as dissolved gas and enabling a more accurate solid–liquid (biphasic) catalysis [9–11]; thus, Gas breakthrough disrupts this interface, reducing activity, meanwhile flow-by maintains it.

These regimes are defined by ΔP across the GDE, in which the precise values are influenced not only by the GDE [20] and electrolyte properties, but also by experimental factors such as GC sampling [11], tubing dimensions, dampers and presence of liquid traps.

Table 1 summarizes published papers applying ΔP to mitigate flooding. Direct comparison is difficult due to inconsistent terminology and differing perspectives across labs. To improve clarity, standardized symbols (defined in the following Eq. (1)) will be used throughout this work and for literature comparison:

$$\Delta P = P_G^{*} - P_L^{*} = P_G - P_L = \text{Differential Pressure} \quad (1)$$

where the acronyms stand for: P* absolute gas/liquid pressions and P for gas/liquid overpressure on GDE.

Among the studies, Ag-based catalysts (reported as one of the most flood-resilient in literature [11]) dominate in terms of stability tests [7,19–21], whatever is the sign of ΔP applied. Many authors suggest applying $\Delta P < 0$ [11,19,20], asserting liquid-side pressure helps guaranteeing flow-by and perspiration conditions, which prevents salt occlusion during time. Different $\Delta P < 0$ values led to perform tests around 200 $mAcm^{-2}$ for several hours [19,20] with an initial selectivity decrease, reaching then a semi-stable production; meanwhile a distinct work declares perspiration helps to minimize the gas product loss through the GDE [11]. For the formers [19,20] the $\Delta P < 0$ condition is induced applying a significant P_G of 345 mbar on the gas side, and higher value for P_L the liquid one, for a large series of GDLs, reporting their pressures tolerance [19,20].

Other studies applied several $\Delta P > 0$, while maintaining $P_L = 0$ references, showing prolonged selectivity [7,18,22], delayed flooding [21], and improved CO_2 diffusion with gas-side overpressure [24], often using buffered electrolytes ($KHCO_3$, K_2SO_4) at ~140–200 mA cm^{-2}.

From these findings, it results that no congruent route exists on optimal ΔP, likely due to differences in experimental setups. Moreover, detailed understanding of how ΔP alters the GDE interface remains limited.

To clarify the flow-by regime and address flooding in MFCs, we systematically investigated how ΔP affects the GDE. GDE behaviour was monitored using pressure sensors, product selectivity tracking, Electrochemical Impedance Spectroscopy (EIS) and Field Emission Scanning Electron Microscopy (FE-SEM). Different setups and derivatized configurations were tested, exploiting several commercial GDLs. We conceived a multi-physics simulation to study multiphase diffusion and capillary-driven electrolyte transport, validating experimental ΔP values.

To mimic and surpass industrial conditions (>200 mA cm^{-2}), all experiments are performed at 0.5 A cm^{-2} using Cu nanoparticles, less flood-resistant catalyst compared to Ag and of fundamental interest for its hydrocarbon production [5,12,25]. Our results revealed an optimized MFC setup where flooding was fully suppressed and high selectivity sustained for 6 h, far surpassing the few minutes typically observed without pressure control. Simulations also provided insight into the pressure-dependent processes occurring within the GDE. These results should be considered independently of the specific activity of the catalyst under analysis, but rather as a key to understanding the phenomena occurring within the GDE to optimize any catalytic process involving GDE.

2. Setup-configuration assembling

Two different setups were evaluated in this work by modifying the movement and connection of liquid and gas flows (*A* and *B*), from them, six different *Configurations* were evaluated during the paper, listed in Table 2. The details of all the employed instrumentations used in the two setups are reported at the end of the paper in the Methodology section. *Setup A* (Fig. S1) is a frequent setup reported in literature characterized by the joining of both the outputs exiting from the cathodic part (gas and liquid) together in the same container [19,22,26–29]. This aspect easily allows the total collection of CO_2RR gaseous products, whether they exit the cell from the liquid or gas side of the GDE. Through the utilization of

Table 1
State of Art about overpressure application on GDE in the CO_2RR field. ΔP values refer to stability test used. Values marked with (*) are not reported explicitly in the paper and are estimated from the SI.

Year	Catalyst	GDL	Current density (mA cm^{-2})	Stability test (h)	Electrolyte	$\Delta P = P_G - P_L$ (mbar)	Ref.
2018	Ag	Covestro GDE	150	800	0.4 M K_2SO_4	20	[7]
2019	Sn	Sigracet SGL-39 BC	100	6	0.5 M $KHCO_3$	0 to 80	[22]
2019	Ag	Sigracet SGL-39 BC	140 to 200	29	2 M $KHCO_3$	>0	[21]
2021	Au	Freudenberg H23C2	–	–	1 M $KHCO_3$	4	[28]
2022	Ag	Toray TGP-H-060, Toray TGP-H-090, Toray TGP-H-120, SGL-22BB, SGL-39BC, ELAT LT1400W, Freundenberg H23C6	<200	20	1 M $KHCO_3$	−70*	[20]
2022	Ag	Toray TGP-H-060, Toray TGP-H-090, Toray TGP-H-120, SGL-22BB, SGL-39BC, ELAT LT1400W	<200	125	1 M $KHCO_3$	−100	[19]
2022	CuO	Freudenberg H23C2	200	75	1 M $KHCO_3$	40, 70, 130	[18]
2023	–	–	–	–	–	−10 to −30	[11]
2025	Cu	SGL-28BC, SGL-38BC, Freudenberg H23C6, Carbon Cloth with MPL	500	12	1 M KOH	15, 30, 50	This work

Table 2
Summary of the different configurations comprehensive of P_G, P_L and ΔP values.

Configuration A0	$P_G = P_L = 0$	ΔP not imposed
Configuration B0	$P_G = P_L = 0$	ΔP not imposed
Configuration A1	$P_G > P_L$	$\Delta P < 30$
Configuration B1	$P_G > P_L$	$\Delta P = 15, 30, 50$
Configuration B2	$P_G < P_L$	$\Delta P \sim 0$
Configuration B3	$P_G = P_L$	$\Delta P = -20$

two BackPressure Controller, it possible to register P fluctuations just outside the gas side (P_G) and the headspace dead volume from liquid side (P_L). Backpressure controller can be used in two ways: it can either monitor pressure variations generated or imposed a constant upstream pressure by opening or closing a valve system to release excess pressure when the set point is reached. *Setup B* (Fig. S2) differs only in the outlet connections for the gas and liquid streams, which are directed to separate reservoirs. P_G and P_L are monitored and governed by separated BackPressure Controllers, thus allowing *gas/liquid breakthrough* and *flow-by* conditions. In the *Optimized- Setup B* (Fig. 1a), a humidifier tank was integrated prior to the gas inlet on the cathodic side, to provide a feed of humidified CO_2. Additionally, a N_2 gas inlet was incorporated into the catholyte reservoir to facilitate the stripping and removal of gaseous products potentially retained within the liquid phase. Fig. 1b shows a photograph of the *optimized Setup B* setup. In all the setups, a three-compartment MFC (Electrocell) able to visualize the back of the GDE was employed (Fig. S3).

From the three different setups presented below, several combinations of configurations are derivatized by reading/applying different values to the P_G and P_L resulting in positive or negative ΔP. A complete list of all the configurations is reported in Table 2. It is important to note that Table 2 shows P as defined in Eq. (1), which should not be confused with the ΔP shown in the same equation.

3. Results and discussion

3.1. Effect of gas-liquid pathway: Configuration A0 and B0

In the first set of experiments, we investigate what is occurring at the GDE interface without applying any P_G or P_L once gas and liquid flows are interconnected (*Configuration A0*) or disjointed (*Configuration B0*). This comparison is fundamental to help untangle the chaotic differences present in the previous literature. Fig. 2a and b illustrates gas product distribution over time along with overpressure variations for *A0*, while Fig. 2c and d respectively for *B0*. Product distribution remained relatively stable during a 50 min experiment, with ethylene being the primary product, reaching a Faradaic Efficiency (FE) of 28 % in *A0* and 25 % in *B0*, and registering a decrease to 10 % in the later one (Fig. 2a, c). Hydrogen was the second most abundant product generated for the system in terms of FE, initially measured at approximately 20 %, with its production progressively increasing for *B0* as the experiment was proceeding. All other detected products, including liquid ones (carbon monoxide, methane, formic acid, and acetate) exhibited FE values below 10 % (see Fig. S4A and C). During 40 min experiment on *A0*, small droplets of electrolyte began to appear on the Carbon Fiber Layer (CFL) of the Sigracet (SGC) electrode used (Fig. S3b). By 51 min, the number of droplets on the back of the electrode had significantly increased, prompting the interruption of the test to prevent the liquid from reaching the backpressure. In contrast, for sample *B0*, the appearance of a smaller number of electrolyte droplets was only observed at 50 min. Regarding performance, the CO_2RR selectivity for *B0* began to decrease after the first 15 min of the test, while for *A0*, the product distribution remained stable (Fig. 2a, c). After 46 min, an anomalous, non-symmetric pressure spike of approximately 50 mbar was observed on the P_G in both models. This disturbance may be associated with the initial stages of flooding; however, it appears to occur primarily in systems operating under ambient pressure.

Considering these last points, a comparison of the P_G readings at the end of the gas flow line and the P_L revealed notable differences between the two models. In *A0*, P_G and P_L are interrelated, influencing each other due to the presence of two connection points: one at the GDE interfaces and another at the reservoir. As shown in Fig. 2b, there is a clear overlap between the observed minima and maxima values, indicating full communication between the two compartments and suggesting a potential mutual influence between the gas and liquid phases. Starting from a lower value of around 10 mbar, the internal pressure fast rises at a value four times higher, suggesting a quite fragility of the GDE. Moreover, it is easy to identify a constant decrease, lasting few seconds, occurring periodically induced by Micro-Gas Chromatography (μ-GC) sampling, corroborating the hypothesis the instrument perturbs the electrolyzer itself [11]. Contrarily, in *B0* where the two flows are separated, the P_G and P_L are fully independent. The P_L shows negligible variation near 0 mbar (thus electrolyte at ambient pressure, showing extremely low-pressure fluctuation within liquid reservoir headspace due to peristaltic pump action), while P_G maintains a stable overpressure of 10–13 mbar. Overpressure values observed on P_G closely align with the initial conditions recorded in *A0*, further suggesting the presence of consistent and inherent perturbations across both configurations (μ-GC sampling).

Both these two base experiments showed flooding failure in a short time scale, thus falling in the category of a "slow" *liquid breakthrough* or a *flow-by* condition characterized by a pronounced perspiration. Moreover, they are the proof of concept for the communication between the gas and liquid sides, thus suggesting the possibility to tune and regulate what is occurring on the GDE's pores by altering the pressures at the interfaces. This implies that only experiments falling inside the same configuration should be compared, an observation that can be extended to previous literature (Table 1).

3.2. Effect of different pressure between gas and liquid sides: Configuration A1, B1, B2 and B3

Considering a baseline P_G oscillating between 10 and 13 mbar in the absence of any externally applied overpressure, a derivatized *B1* experiment was first conducted by applying the smallest possible P_G at 15 mbar at the cell outlet (Fig. 3). The primary objective of this approach was to investigate whether such slight P_G could offset the system-induced depressurization observed in previous experiments (Fig. 2), thereby preventing the registered flooding occurred in the first hour of *B0* test. It is worth considering that the μ-GC sampling itself could cause a partial occlusion of the GDE causing P_G depression at each step. As reported in Fig. 3b, applying a P_G of 15 mbar induces a deeply stable baseline on the gas flow, thus preventing pressure drop caused by the μ-GC (further highlighted by the zoomed P_G inset) and other components. Surprisingly, *B1* with 15 mbar was already able to delay the onset of flooding: during 180 min experiment (3.6 longer compared to *B0*), only minor indications of visual flooding were observed from the back of the electrode (extremely small droplets). These resulted not significant to alter the CO_2RR selectivity until 80–90 min (Fig. 3a). In this case, a decreasing in ethylene production was observed, dropping from 38 % to 31 % FE at final test. Conversely, H_2 production increased from 17 % to 24 % FE, meanwhile CH_4 and CO remained below 10 % FE throughout, with CO showing a slight decline around 80 min, which coincided with a corresponding increase in CH_4 production. Large potential fluctuations (±500 mV average variations) were observed in the Chronopotentiometry (CP) results (Fig. S5d), indicative of increased instability, leading to a more fragile and partially disrupted electrical conductivity across the interface under conditions of $\Delta P > 0$. Liquid products are presented in Fig. S4d.

The unexpectedly high selectivity retention observed under relatively low P_G prompted further investigation into the effects of higher values favouring the gas phase, with the aim of fully suppressing flooding. Based on several screening results, additional *B1* tests were

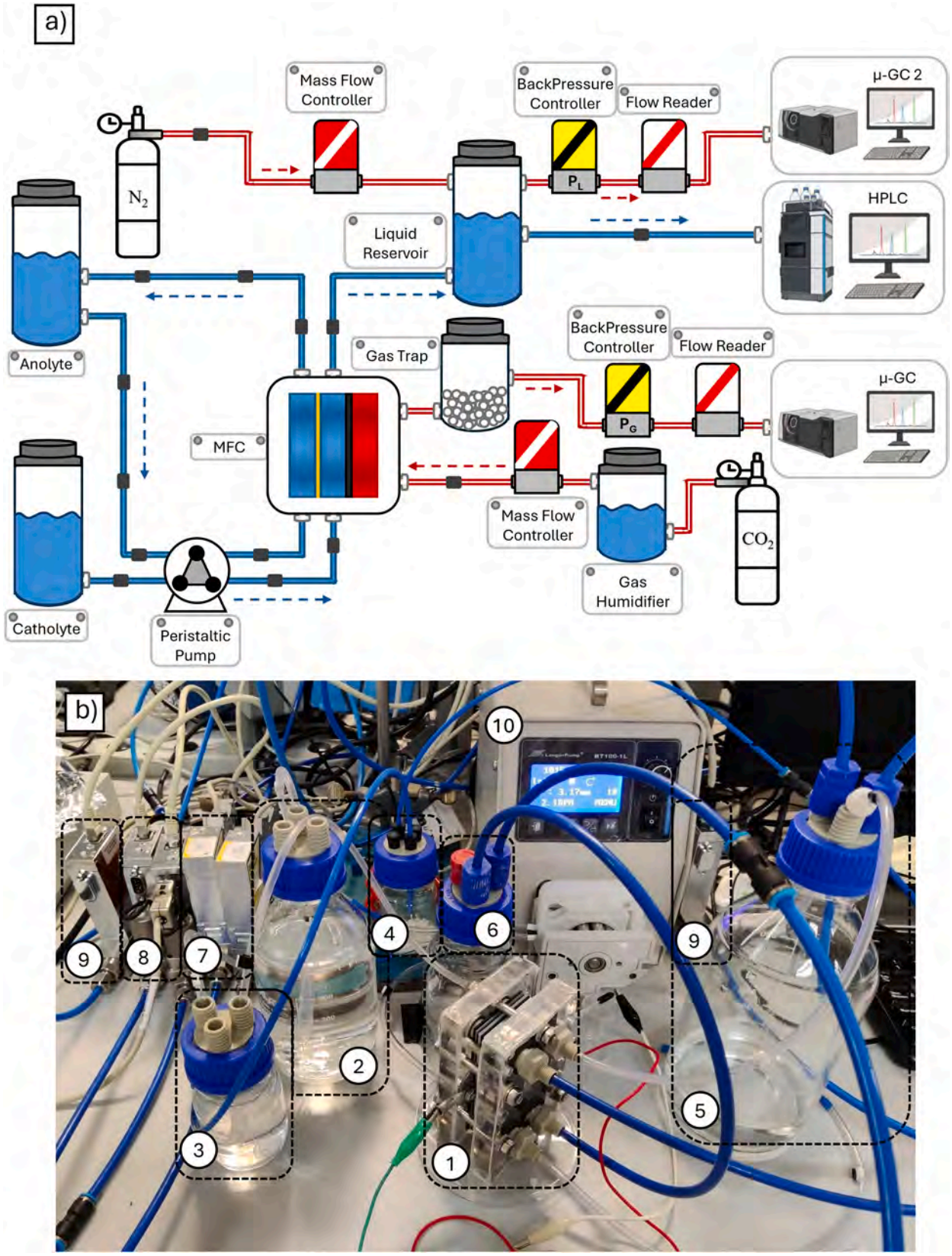

Fig. 1. a) Schematic representation of the optimized setup B, b) experimental setup: 1) MFC; 2) catholyte reservoir; 3) anolyte reservoir; 4) gas trap; 5) liquid reservoir; 6) gas humidifier; 7) BackPressure controllers; 8) MassFlow controllers; 9) FlowReaders; 10) peristaltic pump.

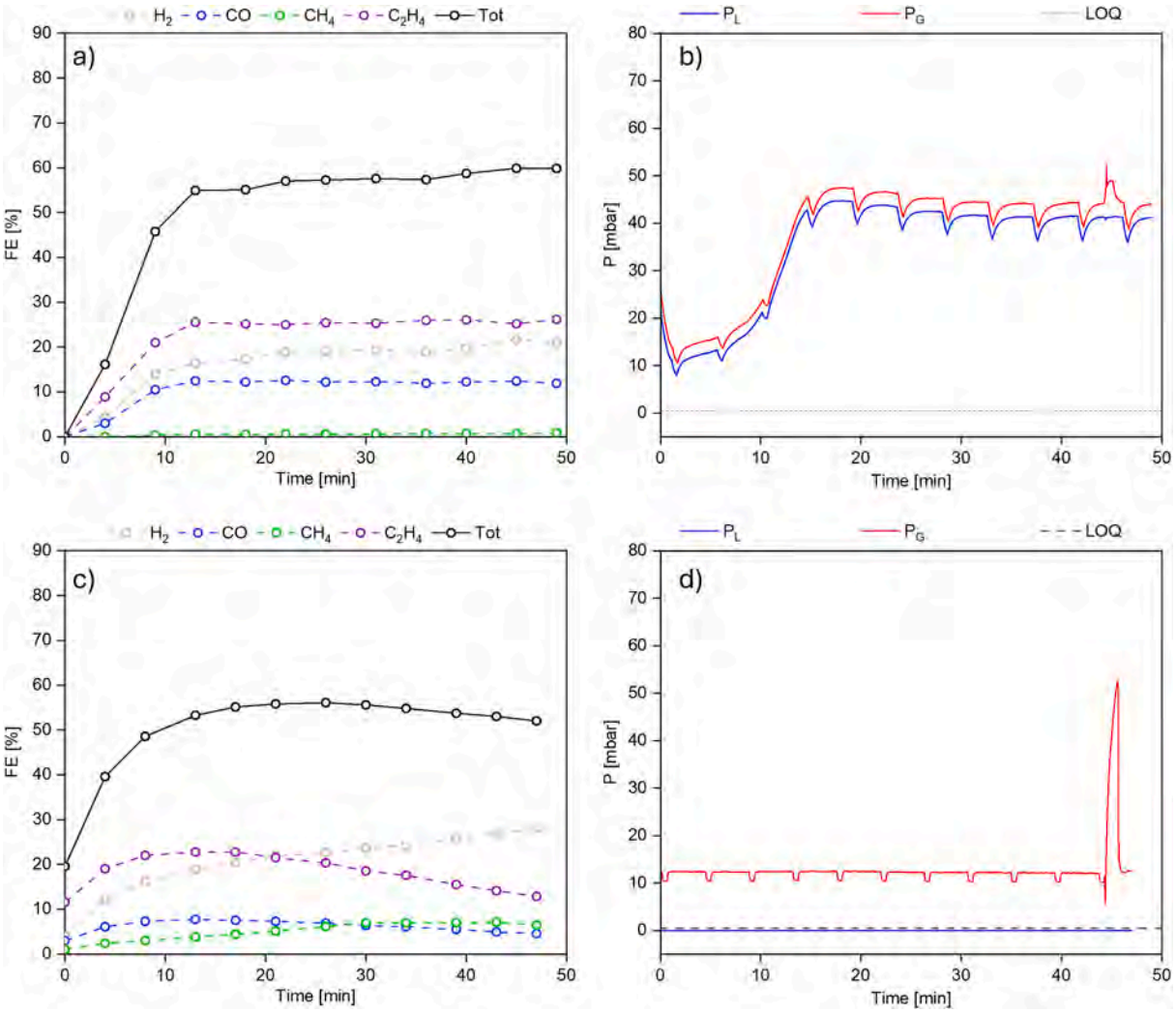

Fig. 2. a) Gas products distribution plotted versus time in *Configuration A0*, b) P_G and P_L read by backpressure controllers in *Configuration A0*. c) Gas products distribution plotted versus time in *Configuration B0*, d) P_G and P_L read by backpressure controllers in *Configuration B0* c. SGC-28BC was employed as GDL. The limit of quantification (LOQ) is defined by the minimum P that the backpressure controllers are able to detect, and being below this threshold, the system registers 0 mbar of P.

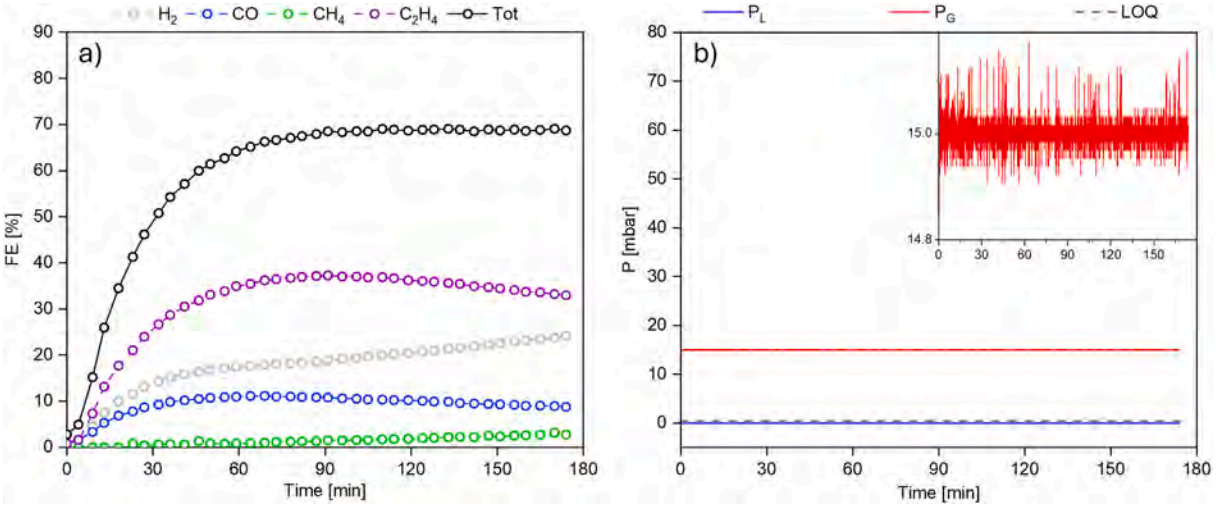

Fig. 3. a) Gas products distribution plotted versus time, b) P_G and P_L read by backpressure controllers in *Configuration B1*. P_G was set at 15 mbar. SGC-28BC was employed as GDL.

performed by increasing P_G to 30 mbar (Fig. 4) and 50 mbar (Fig. S6), assessing whether the onset of flooding could be further delayed and to accurately determine it.

At $P_G = 30$ mbar, *B1* experiment completely prevents flooding on the back of the GDL for a test of 480 min (9.6 time longer compared to *B0*), validating this flooding prevention strategy. Nevertheless, close to the 180 min, from Fig. 4 it is visible a generic decrease for CO_2RR and inverted trend for the HER. Values of ethylene start at 28 % FE until 100 min, decreasing at 10 % FE at 300 min. For HER, 25 % FE was reached until 180 min, where it starts to increase to 37 % reaching its maximum value. CO production starts near 16 % reaching concentration of 4 % at final experiment, meanwhile all other gas and liquid products remained under 10 % FE. Reaching the 360 min of experiment, electrochemical reactions reached a semi stable condition. At $P_G = 50$ mbar, *B1* experiment led to visibly gas bubbles exiting in the liquid side of the GDE, thus leading to *gas breakthrough* condition. Carbon based GDL, such as SGL-28BC, have structural defects in the carbon matrix which can lead to gas permeation with small pressure variations [11]. For the latter experiment, flooding is still prevented, nevertheless, the gas permeation compromises partial loss of gas products into the liquid phase and disruption of the electrical contact between the electrode and the electrolyte. All experimental data supporting this behaviour are provided in the Supporting Information (Fig. S6), as the results obtained at $P_G = 50$ mbar were comparable to those at 30 mbar.

The $P_G = 30$ mbar *B1* experiment, suggest us that flooding prevention in MFCs appears to reduce in any case the mass transport within the pores, probably due to residual perspiration which leads to salt precipitation inside them [6]. This, in turn, results in a gradual decline in CO_2RR selectivity close from 180 min from Fig. 4. Such performance failure was dictated and demonstrated by evident bicarbonate crystallization on the CFL of the GDE by FE-SEM analysis of the spent electrode (showed in Fig. 7 and discussed in Section 3.4). Bicarbonate crystallization is a well-established problem studied on alkaline MEA electrolyzer [30] correlated to the reduced gas feed reaching the catalyst, consequently decreasing product generation. This effect is particularly noticeable as the experiment continued producing detectable products for up to 480 min without any visible signs of flooding over the DL of the GDE, even though with FE approximately 75 % lower than at the initial stage. *B1* experiments evidence how an MFC setup can prevents flooding problems commonly observed on MFC electrolyzer, beside that reaching a catalysis deactivation similar to the MEA electrolyzers.

In order to proof that pressure balance at the interface of the GDE is the main responsible for flooding prevention, and not barely a higher input P_G, a counter evidence experiment was built up by applying a $P_G =$ 30 mbar on the *Configuration A0* (resulting in the new *Configuration A1*, Fig. S1 and Table 2). Being *A1* a merged configuration, P_G is partially transferred to the liquid side of the GDE, thus causing unstable P_L, which slowly increase till flooding failure at 68 min (Fig. S7) (mitigation increased by 1.33 compared to *A0*). Therefore, a stable ΔP is not reached, since P_L has an uncontrollable increase. *A1* experiment evidences how MFC scale up must provide a stable control of the pressure involved, possible only on disjointed gas and liquid flows, as in Setup B.

Configuration B2 ($P_G = P_L$) and *B3* ($P_G < P_L$) were also investigated and reported in the Supporting Info (Figs. S8 and S9). From the previous results, it is easy to see that guaranteeing the same P_G and P_L ($\Delta P = 0$), or even a higher value to the liquid side ($\Delta P < 0$), shortens the lifetime of GDE making the liquid able to fill the gas pores with consequent flooding. Respectively for *B2* and *B3* configuration, an evident flooding occurred after 75 and 51 min. Interesting, these results do not match with the ones coming from reference [5, 6] despite sharing the similar setting of $\Delta P < 0$. However, as previously claimed, we consider these two independent sets of experiments not comparable, being our tests performed on *Setup B* setting, meanwhile the cited papers fall back into *Setup A* type. Moreover, the two set of experiments utilize different GDLs, catalysts and electrolytes, as schematized in Table 1.

The combination of *A1*, *B1-30mbar*, *B1-50mbar*, *B2* and *B3* experiments furnish complete clarification on the GDE interface: ΔP must be balanced between both GDE's sides, only feasible with disjointed gas and liquid flows (discouraging *Setup A* types). Moreover, ΔP should not exceed an edge value to prevent the *gas breakthrough*; a characteristic tailored on the properties of the GDL employed.

3.3. Correlating GDL properties to the applied pressure

From the flooding resolution obtained by inducing a $P_G \geq 15$ mbar and the low resiliency of SGL-28BC on pressure variations (*flow-by* to *gas breakthrough*, switching from 30 to 50 mbar) reported in Section 3.2, we have been encouraged to explore different types of GDLs to realize an optimized MFC with *Configuration B1* type, to enlarge the working pressure range in *flow-by* condition, meanwhile maintaining a stable liquid interface and maximizing the CO_2 dissolution and consequent diffusion.

Among commercial suppliers, we have identified two possible gas porous electrodes that should partially match their properties compared to the SGC-28BC: the SGC-38BC, a thicker variant having identical dispersion and layer composition, and Freudenberg H23C6, which has a comparable thickness to the former, with a distinct structural arrangement and layer dispersion. A fourth class of electrode was studied but

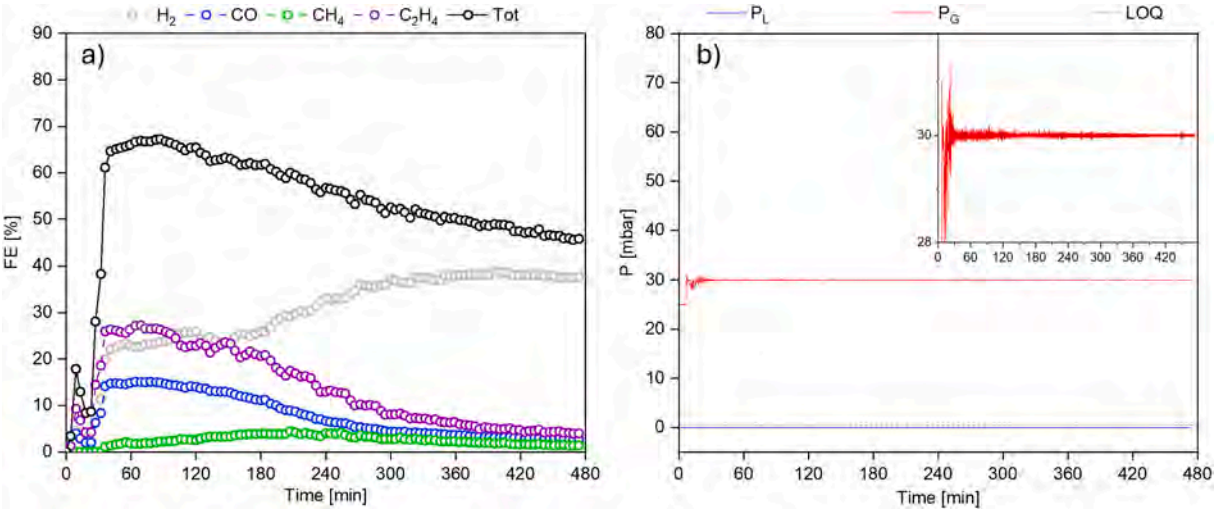

Fig. 4. a) Gas products distribution plotted versus time, b) P_G and P_L read by backpressure controllers in *Configuration B1*. P_G was set at 30 mbar. SGC-28BC was employed as GDL.

not reported in this work, the CT Carbon Cloth with Micro Porous Layer (MPL), which is characterized by extremely larger pores [19,20]: these allow CO_2 bubbles breakthrough without applying any P_G, therefore we decided to omit this electrode from the discussion. The two new GDLs were evaluated with the *Configuration B1* applying P_G of 30 mbar for a duration of 200 min.

In Fig. 5, the results obtained using SGC-38BC are reported. Compared with the analogues results obtained with SGC-28BC, the 38BC selectivity toward ethylene and carbon monoxide values were slightly higher (respectively 35 % FE_{C2H4} and 23 % FE_{CO} compared to 28 % FE_{C2H4} and 16 %FE_{CO} in SGC-38BC at 60 min of experiment). Flooding was prevented also with this GDE, and bicarbonate crystal formation was also evidenced, correlated to the decreasing selectivity toward CO_2RR (Fig. S5i and Section 3.4). Surprisingly, the CO_2RR selectivity drop for 38BC occurred at a later stage compared to 28BC and taking ethylene production as a representative example, the SGC-38BC electrode initially exhibited approximately 35 % FE, which gradually decreased to below 30 % after 150 min of experiment. In contrast, the SGC-28BC electrode began with a lower initial FE of around 28 %, followed by a more pronounced decline starting at 120 min. Moreover, the methane generation was increasing while the experiment was running, reaching a value of 9 % FE, probably due to crystal occlusion which slowly fed the electrolyzer with a lower amount of CO_2. In fact, lower access to CO_2 involves less active site bonded to the former, thus disadvantaging dimerization step for ethylene production [31,32].

Flooding failure in MFC cells employing Sigracet carbon paper electrodes appears to be manageable by applying a P_G. Interestingly, data obtained using Freudenberg H23C6 suggest that flooding cannot be effectively mitigated under the same conditions. As shown in Fig. S10, during the 200-min experiment, CO_2RR activity was sustained only for the initial 30 min, after which visual evidence of flooding was observed on the electrode's CFL, indicating a severe performance limitation. Further information is reported in the Supporting Information (SI§3.2 and Fig. S5j).

We can conclude the physical-chemical properties of GDL have tremendous impact on the pressure interface, which is coherent with the previous literature [19,20]. Interestingly, a further improvement of the liquid-solid interface has been reached with SGC-38BC by evaluating the CP plot (Fig. S5i). During the first minutes of electrolysis, a pronounced oscillation of the potential is recorded, which gradually stabilize around 110 min. We hypothesise that inside the GDE is currently occurring a *flow-by* condition more prone to *gas breakthrough* in the first hour and then prone to *liquid breakthrough*. This implies that an ideal MFC device can be optimally designed with a specific GDE tailored for pressure tolerance. For this reason, from an experimental approach to determinate the ideal P_G value, we have implemented a multi-physical simulation model aiming to determinate the best value considering the physical parameters of the GDL taken into account.

3.4. Multiphysics modelling correlation with experimental values

The relationship between the applied P and flooding of the GDE was investigated using a simplified numerical model. The model was calibrated against experimental conditions to reproduce the operating regime of the electrochemical cell. Material properties, geometry, and boundary conditions were selected to closely reflect the tested system (see Methodology).

Flooding in hydrophobic porous media occurs when the capillary pressure, defined as $P_C = P_G^* - P_L^*$ (with P* intended as absolute pressure, see Eq. (1)), becomes negative and sufficiently large in magnitude, such that the gas pressure is no longer sufficient to resist liquid intrusion. Higher contact angles (θ) inhibit flooding by requiring more negative P_C to initiate liquid penetration. Initially, the CL exhibited a contact angle of approximately 126°, which decreased to below 92° after electrochemical operation (Fig. 6a). Simulations confirmed that flooding does not occur for $\theta \sim 126°$, while significant imbibition is observed below a critical value of $\theta \sim 92°$. To reproduce the gradual loss of hydrophobicity observed experimentally, the simulation time was set to 2 h, with the contact angle decreasing linearly from 126° to 90° over the first 75 min. Time evolution was introduced solely to impose a gradual decrease in contact angle, allowing the system to remain near quasi-steady conditions at each step. This approach avoids the influence of transient effects and dynamic electrochemical responses, such as time-dependent variations in FE, which are beyond the scope of this analysis. The focus is instead on the capillary and gas transport response to changes in wettability and applied P_G, in this section considered as a boundary condition applied at the CFL-gas feed interface (see Methodology).

Fig. 6a shows the electrolyte saturation at the CL-electrolyte interface as a function of θ with boundary $P_G = 0$ mbar. Saturation is defined as the fraction of the pore volume occupied by the electrolyte. A local saturation of 1 indicates pores fully filled with electrolyte, while 0 corresponds to complete dry-out: both extremes are detrimental to GDE performance. Optimal operation occurs at intermediate saturation, where sufficient electrolyte ensures ionic transport and CO_2 reduction, while enough gas volume remains to supply CO_2 and prevent depletion. In general, saturation has a lower limit of $S_0 > 0$, i.e. comprising a residual fluid volume that is bound to the smallest pores and is determined by the microstructure and composition of the considered medium.

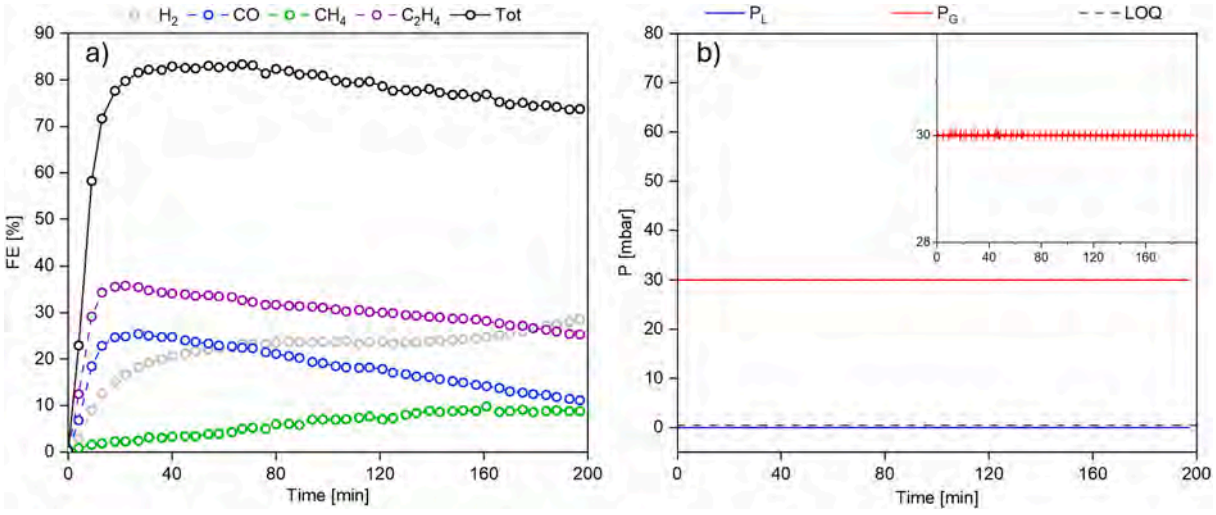

Fig. 5. a) Gas products distribution plotted versus time, b) P_G and P_L read by backpressure controllers in *Configuration B1* configuration was set at 30 mbar. SGC-38BC was employed as GDL.

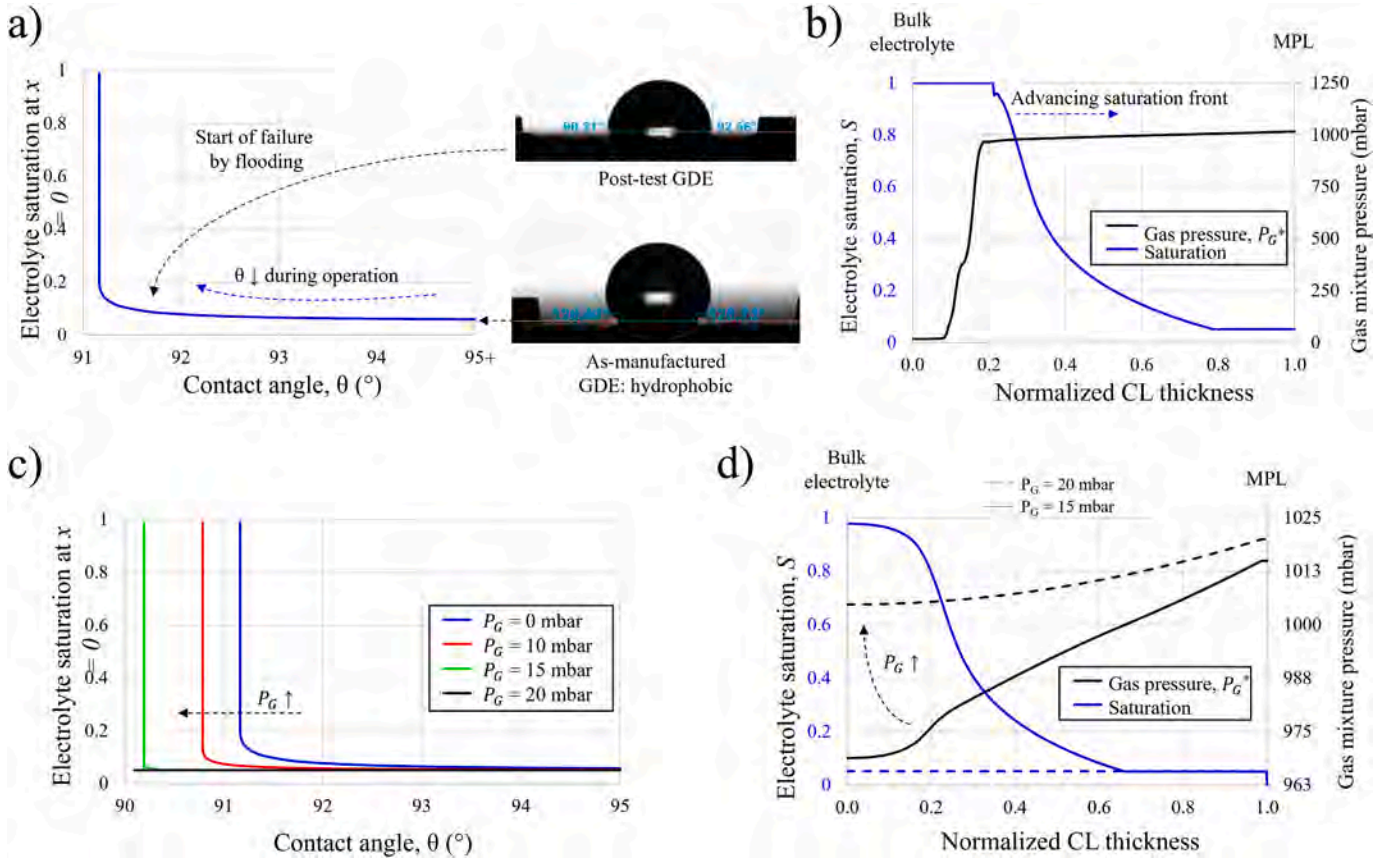

Fig. 6. Results of the numerical model assessing the impact of applied P_G and the CL hydrophobicity on flooding. (a, c) Saturation level at the CL–electrolyte interface as a function of decreasing θ for different applied P_G (c), highlighting the thresholding condition leading to flooding (a). (b, d) Gas pressure (black curves) and saturation (blue curves) in the CL for $P_G = 0$ mbar (b: showing progressing flooding), $P_G = 15$ mbar (d: solid curves, showing flooding initiation), and $P_G = 20$ mbar (d: no flooding). The x-axis was normalized on the CL thickness t_{CL}, with $x = 0$ marking the CL–electrolyte interface, and x = 1 identifying the CL–MPL interface. Note that, in this context, the applied overpressure PG is intended as a boundary condition on the gas feed boundary.

Saturation remains close to S_0 until θ falls below 92°, beyond which a sharp increase in saturation is observed: considering the current operating conditions, flooding is inhibited until a thresholding contact angle is reached, e.g., due to the reduction in the CL hydrophobicity driven by. As θ decreases (as shown in Fig. 6a), the local saturation increases due to the loss of hydrophobicity; as a consequence, the relative gas permeability drops sharply (proportionally to $1 - S^{3.5}$), impeding gas replenishment. Consequently, the continuous CO_2 consumption causes a drop in local gas pressure, further lowering the capillary pressure and accelerating electrolyte invasion (the condition shown in Fig. 6b): a positive feedback loop leading to full flooding.

Among possible strategies to mitigate this process, a P_G was applied at the gas feed, promoting gas permeation throughout the GDE and, therefore, counteracting flooding. As shown in Fig. 6c increasing the applied boundary P_G shifts the flooding threshold to lower θ values (see curves from blue to black): at the limit, applying a P_G of 20 mbar delays flooding to θ ~90°. The effect of the applied boundary P_G on the equilibrium between P_G* and P_L* can be appreciated Fig. 6d, which compares the gas pressure (black curves) and saturation (blue curves) fields for P_G of 15 mbar and 20 mbar (solid and dashed lines, respectively). At $P_G = 15$ mbar, flooding occurs when θ drops below ~ 90.2°, as indicated by the saturation reaching unity at the CL–electrolyte interface, with a gas pressure below 975 mbar. In contrast, at $P_G = 20$ mbar, the gas pressure remains above 1 bar, sufficient to prevent flooding even at θ = 90° (S remains stable at S_0), where liquid permeation would begin for any $P_G < P_L$ at the CL-electrolyte interface.

These results highlight that P_G low as 30 mbar under the studied conditions can stabilize gas transport and mitigate flooding driven by hydrophobicity loss. This outcome aligns with experimental observations, particularly considering that both transport properties and electrochemical parameters of the GDE were calibrated against measured data. The critical P_G threshold depends on the operating conditions and structural properties: higher current densities, larger electrochemical surface areas, or lower absolute permeability increase the CO_2 demand and promote pressure drops, thus requiring higher boundary P_G values. Notably, maintaining minimal saturation (i.e., $S = S_0$) is not necessarily the optimal design objective: high GDE productivity is promoted by maximizing the interfacial area between solid, gas, and liquid phases, which requires a balanced saturation level. Tailoring the microstructure to achieve this balance, while accounting for operational constraints, represents a key optimization pathway. Finally, while the present model assumes progressive electrowetting as the sole cause of θ reduction, other failure mechanisms may arise. In particular, if the CL becomes hydrophilic (θ < 90°), capillary forces favour spontaneous imbibition, and higher boundary P_G would be needed to prevent flooding. Alternatively, low saturation levels can hinder ionic transport, potentially leading to salt precipitation and pore clogging. Although not explicitly modelled here, such effects would further reduce gas permeability, resulting in lower P_G for the same operating condition and, therefore, promote flooding, as experimentally registered in Sections 3.2 and 3.3, other than proofed by visible crystal salt found by FE-SEM (see Section 3.5).

This multiphysical model, despite accounting for only a limited number of physical phenomena and specific features of the GDL, is already capable of accurately capturing the onset of flooding and identifying an optimal P_G value. This strongly suggests that a

multiphysical approach may represent the most effective pathway toward the model-based design of a next-generation GDL with enhanced performance in electrolysis applications, as well as emphasising the importance of this type of study for the development of scaled-up devices.

3.5. Physical and electrochemical evidences of bicarbonate occlusion inside GDE

SEM was employed to investigate structural and morphological changes in the electrodes after the experiments conducted under *flow-by* condition, able to prevent flooding. Imaging was performed on the CL, the backside of the CFL, and electrode cross-sections to determine layer thicknesses and to detect whether pore blockage or limitations in mass transport could be attributed to crystallization phenomena. The characterization data were also incorporated into the modelling software to parameterize the simulations with conditions as close as possible to the experimental setup. In both pristine and post-CP electrodes made from SGC-28BC, 38BC and Freudenberg H23C6 carbon papers were examined.

Both for SGC-28BC and 38 BC, the SEM images of the CFL after the experiment reveals the presence of prominent crystals of varying sizes: for 28BC ranging from approximately 100 μm for the largest to near 10 μm for the smallest (b), for the 38BC only scattered and unevenly distributed crystals across the surface, with an average size of approximately 100 μm (Figs. 7d and S11).

From surface-level appreciation, the quantity of 28BC crystals does not look to be sufficient to completely block the electrode pores or significantly impede gas transport, which is coherent with the experimental data of retained lower selectivity rather than a complete CO_2RR inhibition and coherent with the literature suggesting a residual perspiration inside the electrode; which, differently form MEA, can effectively help to prevent bicarbonate precipitation [21]. In contrast, for 38BC some crystals also appeared to grow within the carbon matrix of the CFL, potentially contributing to pore blockage and hindering gas transport through the electrode. It should be considered that, being an

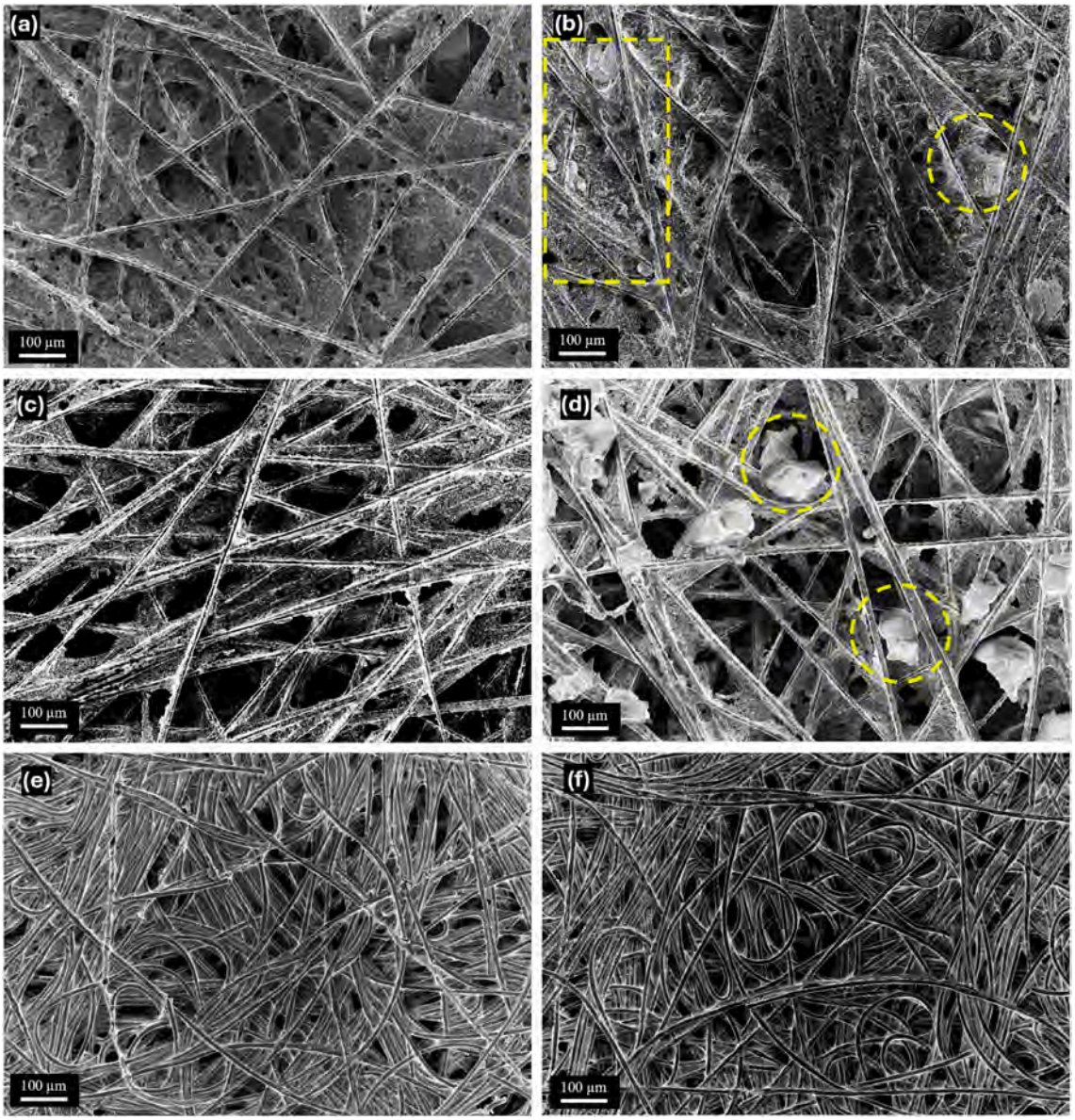

Fig. 7. SEM images CFL before (left) and after (right) reaction of the SGC-28BC (a, b) SGC-38BC (c, d) and Freudenberg H23C6 (e, f) carbon paper.28BC and 38BC were tested at −500 mA cm^{-2} in KOH 1 M for 2 h. H23C6 was tested at −500 mA cm^{-2} in KOH 1 M for 1 h due to flooding. Highlighted regions indicate bicarbonate visible crystallization.

ex-situ characterization after the electrolysis step, by interrupting P_G overpressure and removing the electrode, there will be inevitable partial contact with the liquid electrolyte.

Energy-Dispersive X-ray Spectroscopy (EDX) analysis of both electrodes confirmed the presence of potassium atoms within the crystalline structures, suggesting that they can be composed of $KHCO_3$. For SGC-38BC, EDX mapping was also conducted to identify other elemental composition in a selected area. Potassium was used as a marker for $KHCO_3$ crystallization, carbon (C) for the substrate matrix, and fluorine (F) for the PTFE hydrophobic treatment inherently present in the GDEs (Fig. S11). In Fig. 8, EDX analysis of a cross-section of SGC-38BC confirms the presence of $KHCO_3$ within the internal structure of the GDE. These findings evidence how the crystallization originates from ion permeation through the GDE, leading to pore occlusion that progresses with experiment duration.

Based on the results obtained, pore occlusion due to $KHCO_3$ precipitation appears to occur progressively during the course of the experiments. The migration of potassium ions from the electrolyte into the GDE structure is likely driven by electrostatic attraction toward the cathode, promoted by the applied current [33]. As shown in Fig. 8, the concentration of $KHCO_3$ within the SGC-38BC electrode is noticeably higher than in SGC-28BC. This difference can be attributed to the greater thickness of SGC-38BC, which allows higher tolerance for salt accumulation before complete pore blockage occurs and consequently, performance for CO_2RR decreases.

In the case of CFL of Freudenberg H23C6, being flooded after the test, no evidence of bicarbonate precipitation is reported (Fig. 7f). When comparing the characteristic data of GDEs from the different commercial suppliers and the morphologies generated on the formation of the CL using SEM, this distinct behaviour can be attributed to variations in layer disposition and porosity, which in turn influence the properties of the resulting CL [25]. Although we selected the material with the most similar distribution characteristics, even minimal structural differences appear to have a substantial impact on the ability to mitigate flooding. Furthermore, SEM analysis reveals crack formation in the catalyst layer of both Sigracet materials (Figs. S12 and S13), whereas the Freudenberg electrode maintains a smooth and uniform catalyst surface (Fig. S14).

EIS analysis was performed before and after electrochemical testing to check the change of saturation and availability of the pores of the GDE through an in-situ approach, thus complementing the intrinsic limit of SEM characterization. The measured impedance spectra are reported in the SI (Fig. S15), together with the curves obtained by fitting the data employing the equivalent circuit shown in the inset [34]. In particular, two parameters [35], R_{ct}, related to the movement of charges at electrode/electrolyte interface, and capacitive double layer (C_{dl}), accounting for the accumulation of charges at the same interface and proportional to Electrochemical Active Surface Area (ECSA), were extracted through the fitting procedure and reported in Table 3.

When comparing data obtained with EIS (Table 3), it is noteworthy that for SGC-38BC, characterized by longer stability, the increase of τ has to be attributed only to an increase of charge transfer resistance and not on double layer capacitance, which, contrarily to other samples, remains substantially unchanged. This implies that the ECSA of SGC-38BC does not undergo permanent alterations due to flooding, effectively making this electrode more resilient to the effects of P, and therefore, more stable, as discussed previously. Moreover, being the catalyst in common among all the three different GDL, we can assume that for 28BC C_{dl} increase it is originated from pores enlargement.

Based on the experimental data and characterization parameters, Sigracet carbon papers are then the most effective electrode for mitigating flooding when a P_G below 50 mbar is applied among the electrode been testes in this paper. Under this condition, indicators of flooding are significantly reduced, extending the experiment duration by approximately a factor of four. Among the Sigracet variants, the thicker 38BC version demonstrates better tolerance to the applied P_G compared to the 28BC counterpart, resulting in more stable performance. Furthermore, the 38BC variant also shows better tolerance to $KHCO_3$ crystallization, requiring a higher accumulation of precipitates before CO_2RR activity is hindered.

It is now clear how MFC can operate in a *flow-by* condition while avoiding flooding failure, nevertheless, a slower decrease of CO_2RR selectivity is still occurring due to bicarbonate precipitation inside the GDL pores, evidenced by SEM and EIS techniques. This information suggests us that the optimized MFC configuration suffers of the same failure of MEA electrolyzer, but mostly furnishes some doubts on the real nature of the *flow-by* condition, in which it seems impossible to completely prevent perspiration.

3.6. Optimized MFC compared to alkaline-MEA

Aware by the failure analogies between the optimized MFC and MEA electrolyzer, we have introduced in our optimized *Configuration B1*, bearing the SGC-38BC, a humidified gas flow; a typical procedure employed with MEA electrolyzer. These conditions were also used to define a stability test with the same catalyst and current density (0.5 Acm^{-2}) for a total of 12 h and compare its performance to the one of MEA electrolyzer. Moreover, to completely characterized the final setup of the MFC, the exiting catholyte was purged with an additional N_2 flow and collected to a second μGC to quantify products loss through the GDE (due to partial *gas breakthrough*).

In Fig. 9, the stability test of the MFC setup utilizing humidified CO_2 is reported; in particular, the FEs in Fig. 9a were calculated considering the gas exiting both from the front and the back of the GDE. Comparing to Fig. 5, which utilizes dry CO_2, the gas product distribution indicates that the use of humidified CO_2 leads to enhanced CO_2RR selectivity and prolonged catalytic activity, being primarily attributed to the increased saturation level of the gas phase, which reduces the evaporation rate of the electrolyte, contributing to improved system stability over time. In

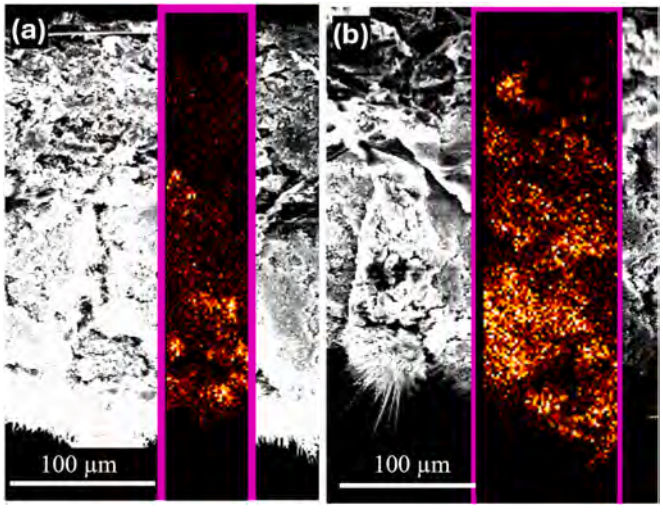

Fig. 8. EDX analysis of the cross-sections a) SGC-28BC and b) SGC-38BC, highlighting the K_α signal of K, representing concentration using a thermal map. Both electrodes were tested at −500 mA cm^{-2} in KOH 1 M.

Table 3
Results of EIS analysis on SGC-28BC, 38BC and Freudenberg H23C6 electrodes before and after the electrochemical tests.

Electrode	Before/after CP	R_{ct} (Ω cm^2)	C_{dl} (mF cm^{-2})	τ (ms)
SGC-28BC	Before	2.02	0.50	1.00
	After	0.81	7.40	6.01
SGC-38BC	Before	0.49	1.27	0.63
	After	1.21	1.24	1.50
Freudenberg H23C6	Before	0.64	0.92	0.59
	After	1.44	1.34	1.92

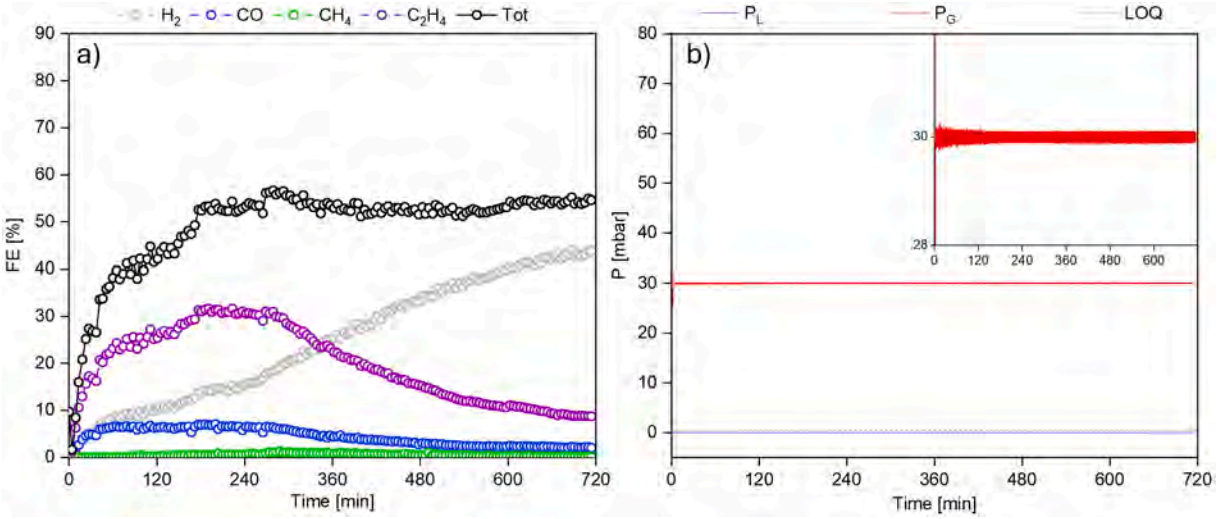

Fig. 9. Stability test of the MFC electrolyzer, a) gas products distribution plotted versus time, b) P_G and P_L read by backpressure controllers in *Configuration B1* setup. P_G was set at 30 mbar. SGC-38BC was employed as GDL.

details, in Fig. 9 ethylene initially exhibited approximately 23 % FE, later increasing to 36 % until pore occlusion (by bicarbonate precipitation) began obstructing CO_2 transport to the active electrocatalytic sites, occurring at 310 min. From that point, ethylene production gradually declined to a minimum of 8 % at 720 min. These results suggest that the system was not flooded because no sign of visual flooding was appreciated over the CFL; rather, the decline in production was solely due to pore occlusion, which limited the total amount of CO_2 available for conversion but did not completely cease the reaction. For the competing H_2 production, it steadily increased throughout the experiment, reaching 43 % FE at 720 min. Meanwhile, carbon monoxide and methane remained relatively stable at 6 % FE and 2 % FE, respectively, until pores occlusion occurred. Thereafter, both decreased to 3 % FE and 0.5 % FE, respectively, due to the reduced CO_2 availability. Liquids products were comparable to previous result (Fig. S4i). As mentioned before, partial gas loss on the liquid side is occurring once referring to the *Configuration B1*, utilizing P_G on the GDE. Previous results reflected a combined contribution of gas-phase products and those released into the headspace from the cathodic liquid. Fig. 10 presents the distribution of individual gas products collected separately from the gas and liquid sides of the GDE during humidified CO_2 experiment.

Interestingly, the analysis of product losses due to *gas breakthrough* and diffusion suggests that approximately 10 % of the carbon-based products were lost. Moreover, given its higher diffusivity, H_2 loss concentration increases in the liquid phase as pore occlusion progressed, while remaining stable in the gas phase. A further experiment validating the current industrial production conditions at 0.2 Acm^{-2} was carried out, investigating a much more significant time scale, exceeding 50 h. In Fig. S19, a 66 h of continuous electrolysis is reported showing similar behaviour: flooding is completely prevented, showing a dry back of the GDE, however, this did not prevent a significant drop in FE_{CO2RR} as the pores became clogged with visible bicarbonate.

Having defined the MFC setup similar to MEA in terms of failure due to bicarbonate precipitation, a final experimental assessment was conducted using an alkaline-MEA setup to allow a comparative analysis with the previously described MFC configuration. Fig. S21a reports FE obtained from experiments performed at a constant current density of 0.5 A cm^{-2} in a 3using the alkaline-MEA setup. Ethylene production initially reached 19 % FE, progressively declining to 8 % by the end of the experiment. In contrast, hydrogen production exhibited an increasing trend, starting at 41 % FE and rising to 73 % at the point of cell failure, a significantly higher value compared to results obtained under MFC conditions. Other carbon-based products remained below 10 % FE throughout the experiment. CO began at approximately 10 % FE

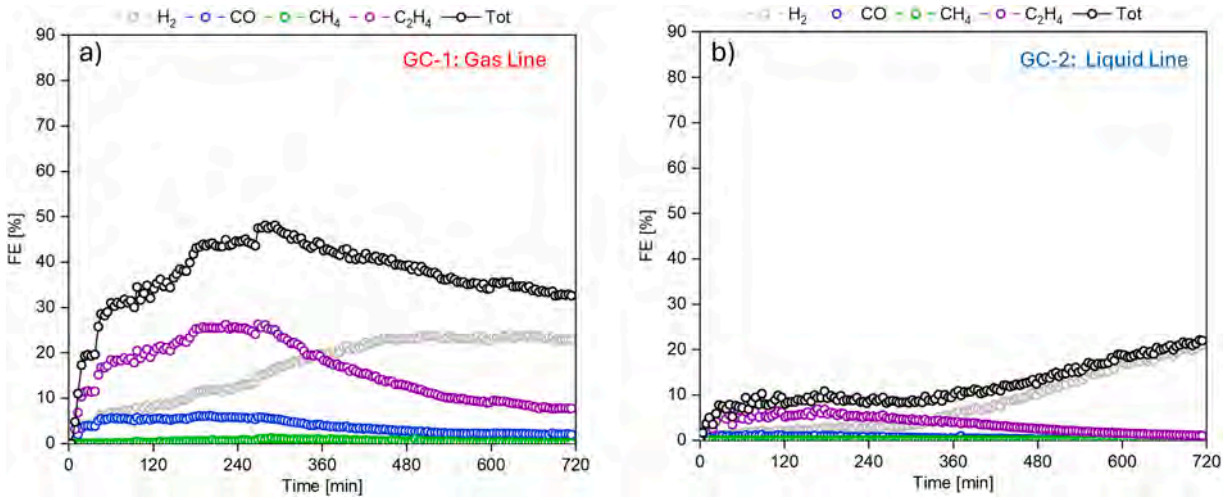

Fig. 10. Gas products distribution versus time coming from the a) gas side of the GDE (back) and b) liquid side of the GDE (front).

with 3 % at final point, while methane started at 0.8 % and rose slightly to 1 % by the end. Notably, methane production increased in the final stages of the experiment, peaking at 1.7 % at 43 min, coinciding with the onset of performance failure due to salt deposition. As a result of this crystallization, the gas serpentine in the cathode compartment became completely blocked, as it can be seen in Fig. S21b showing a decreasing gas flow form the outlet of the cell by time. Such occlusion did not allow CO_2 to reach the catalyst properly and hinders gaseous products removal from the cell. Considering this experiment, the MFC setup showed a more performing electrolyzer in terms of CO_2RR selectivity.

Interestingly, comparing SEM images (Fig. S16) of the electrodes after electrolysis with KHCO3 anolyte, reveal a greater accumulation of crystalline deposits in the alkaline-MEA setup compared to the MFC. Additionally, the morphology and spatial distribution of the crystallized material appear distinctly different. EDX elemental mapping shows bicarbonate crystal formation initiates predominantly at the back side of the CFL where humidified CO_2 is introduced, totally opposite of the MFC electrodes in which is only detectable closest to the CL [36].

Based on the collected and analyzed data, the optimized MFC configuration emerges as the most promising approach for mitigating flooding/crystallization failures. However, the occurrence of partial *gas breakthrough* while working in the *flow-by* condition, highlights the ongoing need for further investigation into GDL materials that can tolerate gas overpressure while maintaining electrode wettability over extended periods, being essential for the realization of a fully optimized MFC system. It should also be noted that, due to the inherent complexity of the experimental setup, this experimental study focused on a defined geometric area of the electrode, thus the scaling size of the cell and the increasing hydrostatic pressure generated by the liquid height should be considered and properly modelled, thus remaining an open avenue for future research and modelling.

4. Conclusions

In conclusion, this paper presents experimental proof of concept, supported by multiphysics modelling, of the causes and consequences of flooding phenomenon on GDE mounted on an MFC, further revealing how its optimization can prevent this failure. The study begins by defining the physics occurring at the GDE interface while managing the gas and liquid side from the cathode combined or separately, moving then to the realization of different ΔP scenario identifying a proper condition to prevent flooding. Such experimental value was validated by a multi physic model, predicting the origin of a second failure: bicarbonate crystal precipitation. Together with SEM and EIS analysis, bicarbonate precipitation was proofed and buffered with an optimized configuration working with humidified CO_2 inlet. This experiment proofed to outperform to several MEA experiments in terms of stability and product selectivity.

This paper clarifies the nature of the physical-chemical phenomena occurring inside the GDE, while highlighting the necessity in the CO_2RR field, besides the MFC/MEA setup, to work in acidic environment to neutralize the intrinsic hydroxide formation caused by the cathodic reaction, thus preventing the unresolvable bicarbonate precipitation.

5. Methodology

5.1. MFC experiments

In all the MFC setups, the electrochemical tests were ran using an electrochemical workstation (Biologic; EC-Lab SP300) on the above described commercial MFC. An Anion Exchange Membrane (AEM) (Fumasep FAB-PK-130) was used to separate the cathodic and anodic sides. The cathodic side was in turn divided into two compartments (liquid and gas ones) by the working GDE with a geometric active area of 0.5 cm^2 (Fig. S17a). An Ag/AgCl (1 mm, leak-free LF-1) was used as the reference electrode and inserted in the catholyte. A Titanium plate covered by a Pt deposition (Electro cell) was used as the counter electrode and immersed in the anolyte. The electrolytes used in the anodic and cathodic part was an aqueous solution of 1 M KOH (84 wt%, Sigma Aldrich) and circulated at 1 mL min^{-1} during the tests. CO_2 was constantly flowing at 30 mL min^{-1} in the cathode gas-pool. *Setup A* is composed by a commercial transparent three-compartment MFC (Electrocell) able to visualize the back of the GDE (Fig. S1), one Mass Flow Controller (Bronkhorst; Max. 200 sccm CO_2), two BackPressure Controller (Bronkhorst; Max. 100 sccm CO_2//0,5 bar, ±0.025 bar) and one FlowReader (Bronkhorst; Max. 100 sccm CO_2) placed in sequence after the BackPressure. The connections were done using plastic tubes (RS; BlueDext, 6 mm diameter) for the gases and transparent plastic tubes for (VWR, 3.17 mm diameter) the liquid electrolytes. A peristaltic pump (Longer Pump BT100-1 L) was used to flow the electrolytes. For the liquid reservoir (and also gas traps of next configuration), glass bottles of 1.0 L, 0.25 L and 0.1 L equipped with plastic caps featuring two or three ports were used. All the gas connections and bottlecaps were tapped with PTFE and leak-checked using a CO_2 Gas detector to prevent gas leakage and obtain constant flow and pressure. In *Setup B* (Fig. S2) the gas outlet is connected to a silica-filled reservoir referred to as Gas Trap, which was designed to prevent liquid entering the gas line and reaching the BackPressure and FlowReader. In the *Optimized-Setup B* a humidifier tank was integrated to provide a feed of upstream-humidified CO_2. A MassFlow Controller (Bronkhorst; Max. 100 sccm N_2), connected to an N_2 line regulated at 2.5 bar, is used to precisely control the N_2 flow rate. Measured flow values are corrected using a factor of 0.7 to convert CO_2-calibrated readings to equivalent N_2 values. About Backpressure controller readings, the following acronyms have been used: differential pressure (ΔP), absolute gas/liquid pressions (P*) and gas/liquid overpressure (P).

5.2. Electrode preparation

For the MFC experiments, the CL was deposited onto the MPL of the GDE by spray coating (Nadetech Spray Coater – Ultrasonic Nozzle) an ink onto three different 6 cm^2 commercially available carbon papers: SGC-28BC and SGC-38BC (from Sigracet SGL Technologies), H23C6 (from Freudenberg) and Carbon Cloth with MPL (Fuel Cell Store). The sprayed ink consisted of 11 mg of CuNPs (40–60 nm particle size, Merck) mixed with 13 μL of a solution containing the ionomeric binder (Sustainion XA-9 5 % in EtOH, Dioxide Materials) in a 4 mL isopropanol solution. The ink was sonicated prior to the deposition for 30 min. Catalyst loading was 1 mg cm^{-2}. From the 6 cm^2 electrode, three smaller pieces of 2 cm^2 were extracted. The front size of the electrode bearing the catalyst layer was then partially covered by PTFE tape exposing a circular section of 0.5 cm^2 of active area (Fig. S17). The diffusion layer was kept completely free at 2 cm^2.

5.3. MEA experiments

Alkaline-MEA system was constructed using a commercial zero-gap MEA electrolyzer (Dioxide Materials) with an active area of 5 cm^2. The cathode GDE (SGC28 BC and 38BC) were prepared by spraycoating Cu NPs with the same procedure of the MFC experiment. While the anode electrode was made of Iridium Oxide (IrO_2) deposited on a Ti felt (285 μm thickness, porosity 50 % from Fuel Cell Store). The pre-treated felt was coated with an ethanol-based solution of Iridium Chloride ($IrCl_4$, Iridium (IV) chloride, 99.95 %, Ir 56.5 min, Thermo Scientific) using a dip-coating technique. After each layer the felt was calcinated in an oven at 450 °C until the target loading of 2.5 mg cm^{-2} was reached. Working in alkaline condition a Sustainion X37-50 Grade RT anion exchange membrane (50 μm thickness, from Dioxide Materials) was used to separate the anode and cathode compartment. The anionic membranes were pre-treated in 1 M KOH overnight and activated in 0.1 M $KHCO_3$. To ensure controlled and optimal compression, the cells were assembled accordingly to the substrate's characteristics. The

compression ratio was optimized to 16 % and 18 % for the 28BC and 38BC separately. Starting with the gasket spacing matching the total thickness of the cathode GDE, and the electrochemical response was evaluated while gradually lowering the cathode gasket thickness. A torque wrench was used to cross tighten each cell bolt first at 2 N m and then at 4 N m. In the anodic compartment, a 0.1 M $KHCO_3$ (Potassium bicarbonate 99.95 %, Sigma Aldrich) electrolyte was continuously recirculated using a peristaltic pump (BT100-L and WT600-1F LongerPump from Drifton) with a flow rate adjusted to 20 mL min^{-1}. While at the cathode, a constant 25 mL min^{-1} flow rate of humidified CO_2 was maintained using a MassFlow controller, while a MassFlow Reader monitored the outlet gas stream, anolyte. Additionally, a Gas Trap system was installed to prevent liquid crossover into the gas line.

5.4. Products quantification

Successively, chronopotentiometry studies were conducted to monitor potential variations over time. All experiments were performed without iR compensation, and potential values were referenced to Reversible Hydrogen Electrode (RHE) using the Nernst equation (Eq. (2)).

$$E_{vsRHE} = E_{vsAg/AgCl} + E_{Ag/AgCl\ (3M\ KCl)} + 0.0591 \times pH \quad (2)$$

Gas-phase products were analyzed by a microGas Chromatograph (μGC, Fusion, INFICON), composed of two channels with a 10 m Rt-Molsieve 5A column and an 8 m Rt-Q-Bond column, respectively, and each channel with a microthermal conductivity detector (TCD). The inlet of μGC was connected to the exit of the FlowReader (cathodic gas chamber) of the electrochemical cell. Liquid-phase products were analyzed post electrolysis by a High-Performance Liquid Chromatograph (HPLC, Shimadzu Nexera ELSD – LTIII), equipped with a permeation chromatography column ReproGel H+ (Dr Maisch 300 × 8 mm) coupled with a Photo Diode Array (PDA) detector and a Refractive Index Detector (RID), with a 5.0 mM H_2SO_4 mobile phase solution (flow rate of 1.0 mL min^{-1}). The HPLC samples were taken at the final point of the experiment and results are expressed as an average overtime.

The faradic efficiency (FE) for each gas-phase product was determined from its concentration in the outlet gas stream, as shown in Eq. (3).

$$FE = \frac{V \times t \times C_G \times n \times F}{V_m \times Q} \quad (3)$$

where V_m is the molar volume of an ideal gas (L mol^{-1}), V is the flow rate of CO_2 at the cathodic side (L min^{-1}), t is the electrolysis time (min), Q is the total charge passed through the system during the electrolysis time t (coulombs, C), C_G is the concentration of the gas product (% v/v), n is the number of electrons required to obtain one molecule of this specific product, and F is the Faraday constant (96,485C mol^{-1}).

The FE for each liquid-phase product was determined from its concentration of a final aliquot taken from the final volume of electrolyte consumed and calculated using Eq. (4).

$$FE = \frac{v \times C_L \times n \times F}{Q} \quad (4)$$

where v is the volume of electrolyte recovered from the outlet of the cathode (L), Q is the total charge passed through the system during the electrolysis (coulombs, C), C_L is the concentration of the gas product (mol L^{-1}), n is the number of electrons required to obtain one molecule of this specific product, and F is the Faraday constant (96,485C mol^{-1}).

5.5. Scanning electron microscopy

The different GDEs were morphologically characterized using FE-SEM, carried out with a Zeiss Supra microscope operating at an accelerating voltage of 5 kV. Images were obtained from the CL to identify potential defects or notable morphological features on the electrode surface. Additionally, images of the DL were taken both before and after electrochemical operation to evaluate morphological changes associated with applied bias or flooding phenomena (see Supporting Info). Cross-sectional FE-SEM and EDX analyses were also conducted to determine the thickness of the different GDE layers and to verify the migration and presence of potassium ions (K^+) within the pore structure as a result of electrolyte permeation caused by flooding. These measurements were conducted in the same Zeiss Supra microscope at an accelerating voltage of 15 kV.

5.6. Electrochemical impedance spectroscopy

Prior to each experiment, EIS was performed to assess the electrode total resistance and ECSA, ensuring the reproducibility of the catalyst layer preparation, thereby maintaining carbon paper and pressure variations in the gas-phase cathodic compartment as the only independent variables. All experiments were carried out at a fixed potential of −1.0 V vs. RHE to ensure adequate polarization of the electroactive species involved in the electrode–electrolyte interface and to optimize the signal-to-noise ratio of the electrochemical data. Measurements conducted under constant current density conditions at −500 mA cm^{-2} exhibited excessive noise, preventing reliable data integration using the employed analysis software (ZSimpWin, EChem Software). Nyquist plots obtained from EIS characterization were analyzed using the software to extract key parameters, including charge transfer resistance (R_{ct}) and double-layer capacitance (C_{dl}), enabling characterization of the interfacial properties and electrode stability.

5.7. Multiphysical simulation assumptions

A multiphysics model was developed using COMSOL Multiphysics® to simulate the GDE behaviour under electrochemical operating conditions. The model focused on pore saturation dynamics, evaluating the pores saturation (S) in relation to variations in the contact angle (θ) of the electrode over time of experiment due to electrowetting. A simplified numerical model of the GDE during operation was developed to investigate the impact of gas pressure on electrolyte flooding. The GDE was represented as a one-dimensional domain comprising the CL, MPL, and the CFL (Fig. S18a). The CL thickness was estimated from cross-sectional SEM-EDX imaging as approximately t_{CL}= 10.7 μm (Fig. S18b). The three layers were assumed to be contiguous, with material properties varying linearly between interfaces.

Structural and transport parameters for the MPL and CFL were taken from manufacturer datasheets. The CL specific surface $a_{v,0}$ was derived from ECSA measurements, yielding approximately 1.27 mF cm^{-2}. Assuming a nominal capacitance of 10 μF cm^{-2} for metallic copper and a CL thickness of 10.7 μm, the resulting specific area was estimated as $a_{v,0} = 1.2{\cdot}10^{-7}$ m^{-1}. This value was used to compute the absolute permeability of the CL via the Kozeny–Carman relation (Eq. (5)):

$$K_0 = \frac{\phi^3}{5(1-\phi)^2 a_{v,0}^2} \quad (5)$$

where $\phi = 0.5$ is the assumed porosity of the CL. The resulting permeability $\sim 7{\cdot}10^{-16}$ m^2 aligns with values reported in the literature [37,38].

Electrochemical reactions were simplified to source/sink terms for gaseous species. The applied current density (i_0 = 500 mA cm^{-2}) was assumed to produce both gaseous and non-gaseous products, based on experimental measurements. The Faradaic efficiency r_i of species i was used to define its corresponding source term (Eq. (6)):

$$\dot{m}_i = \pm i_0 r_i a_{v,0} S \frac{M_i}{nF} \quad (6)$$

where M_i is the molar mass of species i, n is the number of electrons involved in the i-th reduction reaction, F is the Faraday's constant, and S

is the local electrolyte saturation; positive and negative signs are respectively related to source (C_1 and C_2 products, H_2) and sink (CO_2 consumption) terms. S is defined as the fraction of pore volume occupied by electrolyte, with $S = 1$ denoting complete flooding. Note that the active surface area $a_{v,0}$ was further scaled by the local saturation S, reflecting that CO_2 reduction occurs only where gas and electrolyte coexist at the catalyst interface. Faradaic efficiencies were assumed constant across operating conditions, in agreement with experimental observations. The total FE of gaseous products was set to 0.62; the remaining 0.38 was attributed to liquid products, which, for simplicity, were modelled as consuming one CO_2 molecule per two electrons. CO_2 consumption was evaluated from the total C_1 and C_2 products generation. Source terms were set to zero as the CO_2 concentration approached zero to avoid numerical instability.

The model includes three main mass transport mechanisms: multicomponent gas diffusion, to identify the local composition of the gaseous mixture; Darcy flow, to evaluate the gas pressure filed through the GDE; capillary-driven electrolyte transport in the hydrophobic CL. The MPL was modelled as an ideally hydrophobic barrier, impermeable to liquid water. Thus, flooding occurs when the CL becomes fully saturated, suppressing CO_2 access and leading exclusively to H_2 evolution.

Multicomponent diffusion was formulated using the Stefan–Maxwell framework, with mixture-averaged diffusion coefficients. Convection was modelled via Darcy's law, using a composition-dependent gas viscosity and local ΔP. Knudsen diffusion was neglected. Binary gas diffusion coefficients were estimated via the Fuller method [39]. Source terms for CH_4, C_2H_4, H_2, and CO were computed according to the simplified electrochemical model, as described above. The CO_2 sink term accounted for both gaseous and liquid product formation. Mass transport limitations in the liquid phase were neglected. The gas feed was modelled as humidified CO_2 (97.5 % CO_2, 2.5 % H_2O vapor in molar fraction). Local water vapor concentration was used to compute relative humidity, which in turn affected electrolyte evaporation: water vapor partial pressure was modelled via Raoult's law [40]. A no-flow boundary condition at the CL-electrolyte interface was considered.

Gas pressure within the GDE was obtained by solving the gas-phase mass balance, with convective flow governed by Darcy's law and driven by local permeability, porosity, and viscosity. Gas viscosity was evaluated using the Herning–Zipperer method [41,42]. Both permeability and porosity were functions of the local saturation S, coupling gas flow with capillary transport. Gas pressure was fixed at the DL/gas-feed interface; a no-flux condition was imposed at the CL/electrolyte interface.

Electrolyte transport in the CL was modelled using the Richards equation [43], solving the liquid-phase mass balance in terms of saturation S and capillary pressure. A minimum saturation $S_0 = 0.05$ was imposed to reflect partial pre-filling. The capillary pressure $P_C = P_G^* - P_L^*$ was related to saturation through a Leverett J-function closure equation for hydrophobic porous media [44]. Note that, in this section, P_G^* and P_L^* refer to the absolute pressure of the gaseous mixture and the electrolyte, respectively. The electrolyte pressure at the electrolyte–CL boundary was fixed to $P_L^* = 1$ bar. Instead, the boundary gas pressure at the CFL–gas feed interface was set as $P_G^* = 1\ \text{bar} + P_G$, where P_G is a constant boundary overpressure, consistent with the experimental framework. The contact angle was assumed spatially uniform across the CL. Electrolyte evaporation was modelled via Hertz-Knudsen equation [43], considering a specific liquid-gas surface area of $10^{-2}\ a_{v,0}S$ [45]. The liquid pressure was fixed at 1 bar at the CL/electrolyte interface, while a no-flux boundary was set at the CL/MPL interface. For the sake of simplicity, the electrolyte density, viscosity and surface tension were approximated with those of water.

Numerical simulations were conducted in COMSOL Multiphysics using a time-dependent solver. Fig. S18a reports the boundary conditions for the variables solved for. A mesh refinement study determined an optimal element size of $t_{CL}/75$, ensuring convergence while maintaining acceptable computation times. Further information regarding model implementation and the adopted parameters are reported in Supplementary Information (SI§5).

CRediT authorship contribution statement

Santiago Quesada: Writing – original draft, Methodology, Investigation. **Laura Gatti:** Writing – original draft, Investigation. **Matteo Alberghini:** Writing – original draft, Investigation, Funding acquisition, Formal analysis, Data curation, Conceptualization. **Alessio Tommasi:** Writing – review & editing, Formal analysis, Data curation, Conceptualization. **Marco Etzi:** Writing – original draft, Investigation, Formal analysis, Data curation. **Alessio Mezza:** Writing – original draft, Formal analysis, Data curation. **Adriano Sacco:** Writing – original draft, Formal analysis, Data curation. **Fabrizio C. Pirri:** Writing – review & editing, Funding acquisition. **Daniele Sassone:** Writing – review & editing, Writing – original draft, Validation, Supervision, Project administration, Methodology, Investigation, Formal analysis, Data curation, Conceptualization.

Funding sources

This publication is part of the project PNRR-NGEU which has received funding from the MUR – DM 117/2023 and DM 118/2023 and it was developed in the framework of the research activities carried out within the Project "Network 4 Energy Sustainable Transition—NEST", Spoke 4: Clean Hydrogen and Final Use, Project code PE0000021, funded under the National Recovery and Resilience Plan (NRRP), Mission 4, Component 2, Investment 1.3— Call for tender No. 1561 of 11.10.2022 of Ministero dell'Università e della Ricerca (MUR); funded by the European Union—NextGenerationEU.

Declaration of competing interest

All the data supporting this article have been included in the main paper and as part of the Supplementary information.

Appendix A. Supplementary data

Supplementary data to this article can be found online at https://doi.org/10.1016/j.cej.2025.171393.

Data availability

Data will be made available on request.

References

[1] J. Hansen, P. Kharecha, M. Sato, V. Masson-Delmotte, F. Ackerman, D.J. Beerling, P.J. Hearty, O. Hoegh-Guldberg, S.L. Hsu, C. Parmesan, J. Rockstrom, E.J. Rohling, J. Sachs, P. Smith, K. Steffen, L. Van Susteren, K. Von Schuckmann, J.C. Zachos, Assessing "dangerous climate change": required reduction of carbon emissions to protect young people, future generations and nature, PLoS One 8 (12) (2013), https://doi.org/10.1371/journal.pone.0081648.

[2] J. Mertens, R. Belmans, M. Webber, Why the carbon-neutral energy transition will imply the use of lots of carbon, C (Basel) 6 (2) (2020) 39, https://doi.org/10.3390/c6020039.

[3] J. Mertens, C. Breyer, K. Arning, A. Bardow, R. Belmans, A. Dibenedetto, S. Erkman, J. Gripekoven, G. Léonard, S. Nizou, D. Pant, A.S. Reis-Machado, P. Styring, J. Vente, M. Webber, C.J. Sapart, Carbon capture and utilization: more than hiding CO2 for some time, Joule (March 15, 2023) 442–449, https://doi.org/10.1016/j.joule.2023.01.005 (Cell Press).

[4] S. Jin, M. Wu, Y. Jing, R.G. Gordon, M.J. Aziz, Low energy carbon capture via electrochemically induced PH swing with electrochemical rebalancing, Nat. Commun. 13 (1) (2022), https://doi.org/10.1038/s41467-022-29791-7.

[5] A. Mezza, J. Zeng, M. Etzi, D. Sassone, F.C. Pirri, A. Sacco, Evaluating bicarbonate electrolyzer configurations for energy-efficient formate production, Adv. Sustainable Syst. (2025), https://doi.org/10.1002/ADSU.202500098.

[6] Y. Wu, H. Rabiee, X.S. Zhao, G. Wang, Y. Jiang, Insights into electrolyte flooding in flexible gas diffusion electrodes for CO2 electrolysis: from mechanisms to effective mitigation strategies, J. Mater. Chem. A R. Soc. Chem. (May 16, 2024) 14206–14228, https://doi.org/10.1039/d4ta01994f.

[7] Y. Na, M.G. Ha, H.S. Park, H.Y. Park, H.J. Kim, D. Henkensmeier, S.J. Yoo, J. Y. Kim, S.Y. Lee, J.H. Jang, Effect of dual-flow channel structures on electrochemical CO_2 reduction in proton exchange membrane electrolyzers, Front. Energy Res. 10 (2022) 943113, https://doi.org/10.3389/fenrg.2022.943113.

[8] K. Yang, R. Kas, W.A. Smith, T. Burdyny, Role of the carbon-based gas diffusion layer on flooding in a gas diffusion electrode cell for electrochemical CO2 reduction, ACS Energy Lett. 6 (1) (2021) 33–40, https://doi.org/10.1021/acsenergylett.0c02184.

[9] N.T. Nesbitt, T. Burdyny, H. Simonson, D. Salvatore, D. Bohra, R. Kas, W.A. Smith, Liquid-solid boundaries dominate activity of CO2 reduction on gas-diffusion electrodes, ACS Catal. 10 (23) (2020) 14093–14106, https://doi.org/10.1021/acscatal.0c03319.

[10] S. Zhu, T. Li, W. Cai, Bin; Shao, M., CO2 electrochemical reduction as probed through infrared spectroscopy, ACS Energy Lett. (March 8, 2019) 682–689, https://doi.org/10.1021/acsenergylett.8b02525 (American Chemical Society).

[11] H.P. Iglesias van Montfort, S. Subramanian, E. Irtem, M. Sassenburg, M. Li, J. Kok, J. Middelkoop, T. Burdyny, An advanced guide to assembly and operation of CO2 electrolyzers, ACS Energy Lett. (October 13, 2023) 4156–4161, https://doi.org/10.1021/acsenergylett.3c01561 (American Chemical Society).

[12] J.K. Dangbegnon, M. Etzi, J. Zeng, A. Chiodoni, C.F. Pirri, CO 2 electroreduction towards ethylene on copper phosphate-derived catalysts in alkaline flow cell, Cat. Sci. Technol. 15 (7) (2025) 2318–2326, https://doi.org/10.1039/D4CY01365D.

[13] R.W. Atkinson, Y. Garsany, B.D. Gould, K.E. Swider-Lyons, I.V. Zenyuk, The role of compressive stress on gas diffusion media morphology and fuel cell performance, ACS Appl. Energy Mater. 1 (1) (2018) 191–201, https://doi.org/10.1021/ACSAEM.7B00077/ASSET/IMAGES/LARGE/AE-2017-00077T_0009.JPEG.

[14] J.T. Gostick, M.A. Ioannidis, M.W. Fowler, M.D. Pritzker, Pore network modeling of fibrous gas diffusion layers for polymer electrolyte membrane fuel cells, J. Power Sources 173 (1) (2007) 277–290, https://doi.org/10.1016/J.JPOWSOUR.2007.04.059.

[15] Y. Wu, L. Charlesworth, I. Maglaya, M.N. Idros, M. Li, T. Burdyny, G. Wang, T. E. Rufford, Mitigating electrolyte flooding for electrochemical CO2 reduction via infiltration of hydrophobic particles in a gas diffusion layer, ACS Energy Lett. 7 (9) (2022) 2884–2892, https://doi.org/10.1021/acsenergylett.2c01555.

[16] J.A. Abarca, L. Warmuth, A. Rieder, A. Dutta, S. Vesztergom, P. Broekmann, A. Irabien, G. Díaz-Sainz, GDE stability in CO2 electroreduction to formate: the role of ionomer type and loading, ACS Catal. 15 (11) (2025) 8753–8767, https://doi.org/10.1021/ACSCATAL.5C02052.

[17] F. Huq, I. Sanjuán, S. Baha, M. Braun, A. Kostka, V. Chanda, J.R.C. Junqueira, N. Sikdar, A. Ludwig, C. Andronescu, Influence of the PTFE membrane thickness on the CO2 electroreduction performance of sputtered Cu-PTFE gas diffusion electrodes, ChemElectroChem 9 (1) (2022), https://doi.org/10.1002/celc.202101279.

[18] B. Sahin, J.J. Leung, E. Magori, S. Laumen, A. Tawil, E. Simon, O. Hinrichsen, Controlling product distribution of CO2 reduction on CuO-based gas diffusion electrodes by manipulating back pressure, Energ. Technol. 10 (12) (2022), https://doi.org/10.1002/ente.202200972.

[19] L.M. Baumgartner, C.I. Koopman, A. Forner-Cuenca, D.A. Vermaas, When flooding is not catastrophic—woven gas diffusion electrodes enable stable CO2 electrolysis, ACS Appl. Energy Mater. 5 (12) (2022) 15125–15135, https://doi.org/10.1021/acsaem.2c02783.

[20] L.M. Baumgartner, C.I. Koopman, A. Forner-Cuenca, D.A. Vermaas, Narrow pressure stability window of gas diffusion electrodes limits the scale-up of CO2 electrolyzers, ACS Sustain. Chem. Eng. 10 (14) (2022) 4683–4693, https://doi.org/10.1021/ACSSUSCHEMENG.2C00195/SUPPL_FILE/SC2C00195_SI_002.XLSX.

[21] M. Duarte, B. De Mot, J. Hereijgers, T. Breugelmans, Electrochemical reduction of CO2: effect of convective CO2 supply in gas diffusion electrodes, ChemElectroChem 6 (22) (2019) 5596–5602, https://doi.org/10.1002/CELC.201901454.

[22] B. De Mot, J. Hereijgers, M. Duarte, T. Breugelmans, Influence of flow and pressure distribution inside a gas diffusion electrode on the performance of a flow-by CO2 electrolyzer, Chem. Eng. J. 378 (2019) 122224, https://doi.org/10.1016/J.CEJ.2019.122224.

[23] Z. Coady, S.G.H. Brookes, Z. Shen, B.J. Rhodes, G. Mapstone, Z. Xu, W. Yu, H. Nishihara, C. Schran, A. Michaelides, A.C. Forse, Unexpected oversolubility of CO2 measured at electrode–electrolyte interfaces, J. Am. Chem. Soc. (2025), https://doi.org/10.1021/JACS.5C09712.

[24] M.C.O. Monteiro, S. Dieckhöfer, T. Bobrowski, T. Quast, D. Pavesi, M.T.M. Koper, W. Schuhmann, Probing the local activity of CO 2 reduction on gold gas diffusion electrodes: effect of the catalyst loading and CO 2 pressure, Chem. Sci. 12 (47) (2021) 15682–15690, https://doi.org/10.1039/D1SC05519D.

[25] M. Etzi, J. Dangbegnon, A. Chiodoni, C.F. Pirri, Impact of gas diffusion layer architecture on the performances of Cu-based electrodes for CO2 electroreduction to ethylene in flow reactors, J. CO_2 Util. 83 (2024) 102772, https://doi.org/10.1016/J.JCOU.2024.102772.

[26] M.E. Leonard, L.E. Clarke, A. Forner-Cuenca, S.M. Brown, F.R. Brushett, Investigating electrode flooding in a flowing electrolyte, gas-fed carbon dioxide electrolyzer, ChemSusChem 13 (2) (2020) 400–411, https://doi.org/10.1002/cssc.201902547.

[27] D. Sassone, J. Zeng, M. Fontana, M.A. Farkhondehfal, C.F. Pirri, S. Bocchini, Highly dispersed few-nanometer chlorine-doped SnO2 catalyst embedded in a polyaniline matrix for stable HCOO-production in a flow cell, ACS Appl. Mater. Interfaces 14 (37) (2022) 42144–42152, https://doi.org/10.1021/ACSAMI.2C12428/ASSET/IMAGES/LARGE/AM2C12428_0007.JPEG.

[28] D. Sassone, J. Zeng, M. Fontana, A. Sacco, M.A. Farkhondehfal, M. Periolatto, C. F. Pirri, S. Bocchini, Polymer-metal complexes as emerging catalysts for electrochemical reduction of carbon dioxide, J. Appl. Electrochem. 51 (9) (2021) 1301–1311, https://doi.org/10.1007/S10800-021-01585-7/FIGURES/6.

[29] P. Jeanty, C. Scherer, E. Magori, K. Wiesner-Fleischer, O. Hinrichsen, M. Fleischer, Upscaling and continuous operation of electrochemical CO2 to CO conversion in aqueous solutions on silver gas diffusion electrodes, J. CO_2 Util. 24 (2018) 454–462, https://doi.org/10.1016/J.JCOU.2018.01.011.

[30] M. Sassenburg, M. Kelly, S. Subramanian, W.A. Smith, T. Burdyny, Zero-gap electrochemical CO2 reduction cells: challenges and operational strategies for prevention of salt precipitation, ACS Energy Lett. 8 (1) (2023) 321–331, https://doi.org/10.1021/acsenergylett.2c01885.

[31] C. Zhan, F. Dattila, C. Rettenmaier, A. Herzog, M. Herran, T. Wagner, F. Scholten, A. Bergmann, N. López, B. Roldan Cuenya, Key intermediates and Cu active sites for CO2 electroreduction to ethylene and ethanol, Nat. Energy (2024), https://doi.org/10.1038/s41560-024-01633-4.

[32] B. Zhang, J. Zhang, P. An, Z. Su, Q. Wan, X. Tan, L. Zheng, Steering CO2 electroreduction toward methane or ethylene production, Nano Energy (2021) 88, https://doi.org/10.1016/j.nanoen.2021.106239.

[33] S. Hao, A. Elgazzar, N. Ravi, T.U. Wi, P. Zhu, Y. Feng, Y. Xia, F.Y. Chen, X. Shan, H. Wang, Improving the operational stability of electrochemical CO2 reduction reaction via salt precipitation understanding and management, Nat. Energy 10 (2) (2025) 266–277, https://doi.org/10.1038/s41560-024-01695-4.

[34] J. Zeng, M. Mignosa, N.B.D. Monti, A. Sacco, C.F. Pirri, Engineering copper nanoparticle electrodes for tunable electrochemical reduction of carbon dioxide, Electrochim. Acta (2023) 464, https://doi.org/10.1016/j.electacta.2023.142862.

[35] J. Zeng, M. Castellino, M. Fontana, A. Sacco, N.B.D. Monti, A. Chiodoni, C.F. Pirri, Electrochemical reduction of CO2 with good efficiency on a nanostructured Cu-Al catalyst, Front. Chem. (2022) 10, https://doi.org/10.3389/fchem.2022.931767.

[36] A.B. Moss, S. Garg, M. Mirolo, C.A. Giron Rodriguez, R. Ilvonen, I. Chorkendorff, J. Drnec, B. Seger, In operando investigations of oscillatory water and carbonate effects in MEA-based CO_2 electrolysis devices, Joule 7 (2) (2023) 350–365, https://doi.org/10.1016/j.joule.2023.01.013.

[37] P. Adesina, J.W. Ager, A.A. Lapkin, Beyond Butler-Volmer equation for CO2 electro-reduction on Cu-based gas diffusion electrodes, Chem. Eng. J. 513 (2025) 162240, https://doi.org/10.1016/J.CEJ.2025.162240.

[38] I.V. Zenyuk, E. Medici, J. Allen, A.Z. Weber, Coupling continuum and pore-network models for polymer-electrolyte fuel cells, Int. J. Hydrog. Energy 40 (46) (2015) 16831–16845, https://doi.org/10.1016/J.IJHYDENE.2015.08.009.

[39] E.N. Fuller, P.D. Schettler, J.C. Giddings, New method for prediction of binary gas-phase diffusion coefficients, Ind. Eng. Chem. 58 (5) (1966) 18–27.

[40] M. Alberghini, M. Morciano, M. Fasano, F. Bertiglia, V. Fernicola, P. Asinari, E. Chiavazzo, Multistage and passive cooling process driven by salinity difference, Appl. Sci. Eng. 6 (11) (2020). https://www.science.org/doi/10.1126/sciadv.aax5015?url_ver=Z39.88-2003&rfr_id=ori:rid:crossref.org&rfr_dat=cr_pub%20%200pubmed.

[41] A. Lee, B. Eakin, Gas-phase viscosity of hydrocarbon mixtures, Soc. Pet. Eng. J. 4 (3) (1964) 247–249.

[42] H. Li, Ø. Wilhelmsen, Y. Lv, W. Wang, J. Yan, Viscosities, thermal conductivities and diffusion coefficients of CO2 mixtures: review of experimental data and theoretical models, Int. J. Greenh. Gas Con. (2011) 1119–1139, https://doi.org/10.1016/j.ijggc.2011.07.009 (Elsevier Ltd).

[43] M. Alberghini, S.V. Boriskina, P. Asinari, M. Fasano, Characterisation and modelling of water wicking and evaporation in capillary porous media for passive and energy-efficient applications, Appl. Therm. Eng. (2022) 208, https://doi.org/10.1016/j.applthermaleng.2022.118159.

[44] J.T. Gostick, M.W. Fowler, M.A. Ioannidis, M.D. Pritzker, Y.M. Volfkovich, A. Sakars, Capillary pressure and hydrophilic porosity in gas diffusion layers for polymer electrolyte fuel cells, J. Power Sources 156 (2) (2006) 375–387, https://doi.org/10.1016/j.jpowsour.2005.05.086.

[45] J. Osiewacz, M. Löffelholz, B. Ellendorff, T. Turek, Modeling mass transfer limitations driven by electrowetting in electrochemical CO2 reduction at silver gas diffusion electrodes, J. Power Sources (2024) 603, https://doi.org/10.1016/j.jpowsour.2024.234430.